Spring 2016

A Hybrid Position Feedback Controller for Bistable Structures

Mehmet R. Simsek
Old Dominion University

A HYBRID POSITION FEEDBACK CONTROLLER FOR BISTABLE STRUCTURES

by

Mehmet R. Simsek
B.Eng. August 2011, Bochum University of Applied Science
B.S. August 2012, Kocaeli University

A Thesis Submitted to the Faculty of
Old Dominion University in Partial Fulfillment of the
Requirements for the Degree of

MASTER OF SCIENCE

MECHANICAL ENGINEERING

OLD DOMINION UNIVERSITY
May 2016

Approved by:

Onur Bilgen (Director)

Thomas E. Alberts (Member)

Drew Landman (Member)

ABSTRACT

A HYBRID POSITION FEEDBACK CONTROLLER FOR BISTABLE STRUCTURES

Mehmet R. Simsek
Old Dominion University, 2016
Director: Dr. Onur Bilgen

Bistability is the property of structures showing the ability to attain two statically stable states. Due to dynamic and static advantages such as no energy demand at stable positions and providing higher deflections compared to a monostable structure, bistability may be appealing in control surface design for aircraft structures and load alleviation for wind turbine blades. The dynamics of bistable structures is nonlinear because of the snap-through occurring during the cross-well oscillation between two stable states. A new control strategy called hybrid position feedback control is developed based on the conventional positive position control to exploit linear dynamics of bistable structures around stable equilibrium positions.

In this thesis, complementary stability, performance and energy analysis of bistable structures controlled by the hybrid controller are investigated using numerical time domain and frequency methods. The stability regions, energy variance by parameters, and the operational regions providing state transition are determined. As a result of the analyses, two alternative design options are proposed and necessary stability regions are indicated.

In addition, experimental analysis is conducted on an unsymmetric cross-ply bistable composite plate to show the feasibility of the hybrid control strategy. Various analyses such as stability and energy consumption are performed.

To my family,
for their support in every step of my life.

ACKNOWLEDGMENTS

First, I am deeply grateful to my advisor Dr. Onur Bilgen for his guidance, patience and support throughout my research.

Sincere thanks to Dr. Drew Landman and Dr. Thomas E. Alberts for being in my committee and for their helpful suggestions.

I would like to thank to Dr. Thomas E. Alberts and Dr. Brett Newman for their instruction in the Controls and Dynamics Courses. I learned many useful tools that I applied to my research.

Thanks to my colleagues in the Smart Systems Laboratory for their comments on my research in our group meetings.

Thanks to the Department of Mechanical and Aerospace Engineering and Dr. Sebastian Bawab for funding the Smart Systems Laboratory in which this research took place. Finally, I would like to acknowledge the financial support from the *Türk Silahlı Kuvvetleri* (Turkish Armed Forces) that makes my education in the U.S. possible.

TABLE OF CONTENTS

Page

LIST OF FIGURES

Figure Page

Figure Page

Figure Page

LIST OF TABLES

CHAPTER 1:
INTRODUCTION AND LITERATURE REVIEW

Since the discovery of the piezoelectric effect on substances such as Quartz, Tourmaline and Rochelle salt, the improvements in operating temperature and solubility property led to the discovery of modern ferroelectric piezoceramic materials, namely, barium-titanate and lead-zirconate-titanate. An actuation device, called the Macro-Fiber Composite, is developed using these piezoceramic fibers and used in various engineering applications [1]. The simplicity of the implementation of MFCs in structures and its actuation capability increase their use in adaptive systems. In addition, they are useful in morphing structures since they can be applied as one piece and avoid the need for extra parts such as hinges and joints.

Bistable structures have been studied recently by various researchers since they have useful applications in adaptive structures. Most of the attention is given to structural and dynamic properties. Additionally, significant attention is given to actuate bistable structures with MFC actuators by using static and harmonic excitation. However, the literature lacks a control scheme, which will help improve the limited actuation capacity of MFCs to control bistable structures. This thesis plans to fill this gap by analyzing a hybrid position feedback control strategy.

1.1. Bistability and its Applications

Bistability is the characteristics of structures exhibiting the ability to adopt two distinct stable positions [2]. These types of structures are preferred for use in morphing applications since they do not require energy when at their stable positions [3]. In addition, due to two distinct configurations, the structure shows two different characteristics in terms of stiffness and damping. This characteristic can be achieved by procedures such as unsymmetrical lamination [4], tailored lay-up [5], pre-stressed cylinder [6], fiber-prestressing [7] and thickness variation [8]. Figure 1-1, shows the two stable equilibrium configurations of a bistable plate.

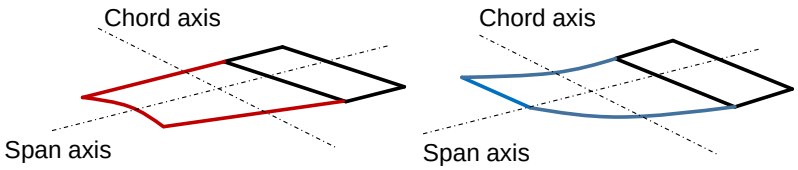

Figure 1-1: Equilibrium configurations of a bistable plate.

The bistable plate consists of an unsymmetric stacking sequence. Bistability occurs due to thermal stresses that occur during the cooling down process by having a different coefficient of thermal expansion for different layers. As can be seen in Figure 1-2, a curvature is induced in both stable states.

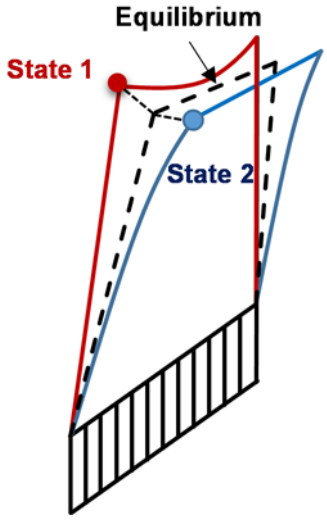

Figure 1-2: An example bistable structure.

The potential energy characteristic of an ideal bistable structure is shown in Figure 1-3. Bistable structures have two potential energy wells around the stable equilibrium positions and an unstable equilibrium point in between. The structure with no velocity stays stable at these stable positions without requiring additional energy. This property makes the bistable structures desirable compared to monostable ones requiring force to maintain position when it is morphed. Depending on the distance of the unstable equilibrium positions, the bistability might be symmetric or unsymmetric. Also, the depth of the energy wells around stable equilibriums might be different depending on the stiffness of the plate for that equilibrium.

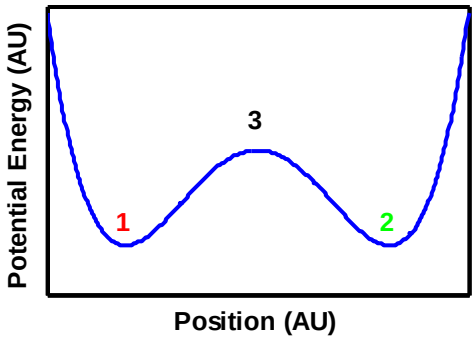

Figure 1-3: Potential energy level of an ideal bistable structure.

These properties of a bistable structure attract research in morphing and adaptive structures. Some of the research focuses on the aerodynamic use of bistable structures. Specifically, bistable structures are considered in morphing wing design of small scale Micro Aerial Vehicles (MAVs) or Unmanned Aerial Vehicles (UAVs). Bistable structures can be used in such applications that require two essential properties: aerodynamic load carrying capacity and a morphing property. The first property requires a bistable structure to have enough rigidity at its bistable equilibrium positions. The second property, morphing, requires an efficient method of actuation of the structures. A bistable plate should show a bidirectional snap-through property since its two different surface properties are necessary during flight. The availability of two shapes enables the aircraft to reduce lift force in gust conditions. Both forward and backward snap-through are essential for aerodynamic applications.

Some of the research conducted in this field is listed as follows. Dano and Hyer [9], developed the theory and experimented with the snap-through mechanisms on unsymmetric composite laminates using the shape memory alloy (SMA) actuator. Schultz et al. [10], studied the snap-through on two-layer cross-ply $[0/90]_T$ laminates utilizing the MFC actuator. Snap-through is achieved only in one direction under the static actuation. Arietta et al. [11] and Senba et al. [12] studied the dynamic property of bistable plates and showed an effective actuation strategy. Then, Arrieta et al. [11] showed dynamically triggered snap-through by exploiting the harmonic oscillation in a way to increase the authority of the MFC actuator. However, the snap-through was only in the forward direction and the actuator was not able to provide reverse snap-through. Senba et al. [12] achieved reverse snap-through with a larger MFC actuator, but it is not practical to have a large actuator on wing-like structures.

Another potential application of bistable morphing structures is the active and passive load alleviation of wind turbine blades. The challenge in wind turbines is high bending stresses and fatigue failure due to the large loads caused by the fluid-structure interaction. The morphing concept can be a solution for this challenge, since in the case of a gust, morphing turbine blades can change their shape so that the excessive load on the blade surfaces can be alleviated.

1.2. The Hybrid Position Feedback Controller

A hybrid position feedback control is proposed by Bilgen et al. [13] to enable bidirectional cross-well transition of bistable structures. The controller is designed based on the dynamics of the stable equilibrium positions of the bistable structure around which it exhibits linear behavior for small perturbations. The proposed method first achieves controller destabilization to make the structure move away from one stable equilibrium position, and subsequently stabilize in the other stable equilibrium position. The proposed collective hybrid control mechanism employs the well-known Positive Position Feedback (PPF) controller and its modified version, the Negative Position Feedback (NPF) controller. The block diagram of the proposed hybrid controller is represented in Figure 1-4.

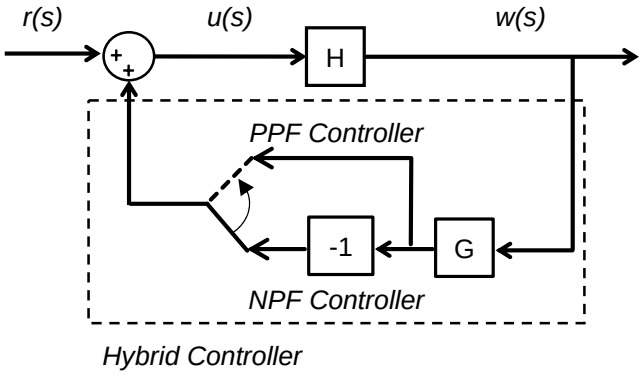

Figure 1-4: Hybrid controller block diagram.

First, the NPF controller is used to induce a controlled cross-well transfer by making the PPF controller intentionally unstable. In the unstable mode, where the feedback multiplier is "-1", the dynamic stiffness of the system is minimized automatically by the controller causing a

typical oscillatory behavior with increasing amplitude. As soon as the unstable equilibrium is reached, the feedback multiplier is set to "+1" causing the controller to be stable.

Figure 1-5 illustrates the cross-well motion of the bistable structure with the hybrid controller. In the figure, the stable states of the bistable structure are labeled S1 and S2. The current position and the unstable equilibrium position are represented by w and w_{u0} respectively.

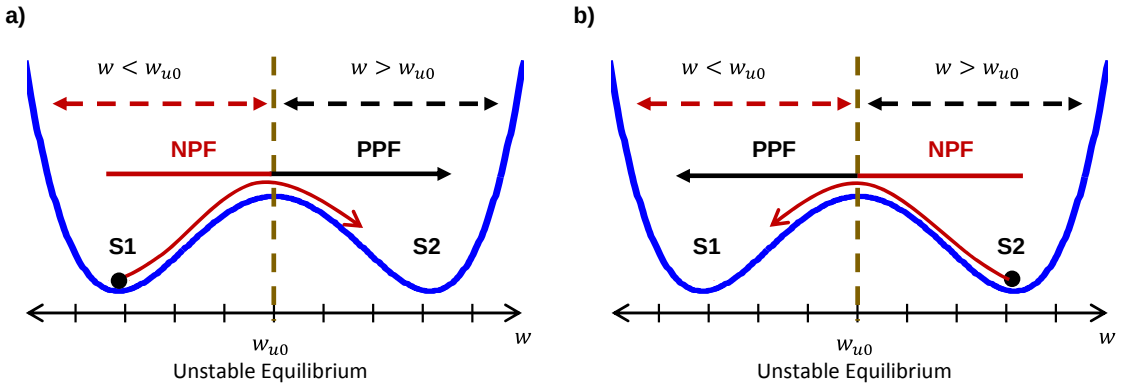

Figure 1-5: State transfer illustration a) from state 1 to 2, b) from state 2 to 1.

For the state transfer from state 1 to 2, the structure is destabilized around equilibrium position S1 by using the NPF mode of the HPF controller. Due to the destabilization, the structure starts an increasing amplitude oscillation around the first equilibrium position. Once the amplitude reaches the unstable equilibrium, the structure snaps towards the second stable equilibrium position. The cross-over is detected by an internal logic and the controller mode is switched to the PPF to attenuate the response around the target state of 2.

1.3. The Position Feedback Controller

As illustrated in Figure 1-6 (a), the PPF control algorithm introduces a second-order filter (G) to the structure (H), which is fed by the sensed position signal. The position response of the filter is then fed back to give the force input to the structure. The NPF works similarly except the feedback is negative as shown in Figure 1-6 (b).

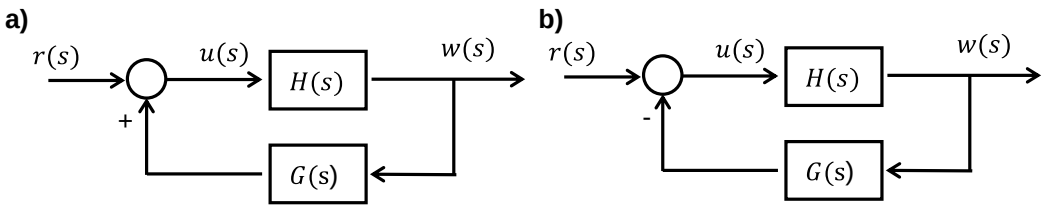

Figure 1-6: Block diagrams of the a) PPF, b) NPF controllers.

In Figure 2, r is the reference signal, and u corresponds to the control voltage to the actuator. The coupled system equations become,

$$\ddot{w} + 2\zeta_n\omega_n\,\dot{w} + {\omega_n}^2 w = g\,{\omega_n}^2\,u \tag{1.1}$$

$$\ddot{u} + 2\zeta_f\omega_f\,\dot{u} + {\omega_f}^2 u = g_f\,{\omega_f}^2\,w \tag{1.2}$$

where g_n is the structure input gain. The actual value of input gain $g_n\,{\omega_n}^2$ is not constant as the voltage/strain level changes, which is confirmed in Bilgen et al. [14] and also discussed by Crawley and Anderson [15]. An average g_n value is found experimentally. The controller parameters ζ_f and ω_f correspond to damping ratio and natural frequency of the controller, respectively. The control gain is denoted as g_f, and it is simply a proportional amplification of the feedback signal. The transfer functions of the structure and controller in Laplace form are given by:

$$H(s) = \frac{g\,{\omega_n}^2}{s^2 + 2\zeta\omega_n\,s + {\omega_n}^2} \tag{1.3}$$

$$G(s) = \frac{g_f\,{\omega_f}^2}{s^2 + 2\zeta_f\omega_f\,s + {\omega_f}^2} \tag{1.4}$$

The two second-order systems form a simple 2DOF system. The PPF controller, in its conventional (stable) setup acts as a simple mechanical vibration absorber. To achieve a cross-well transfer, the PPF controller is intentionally made unstable by modifying it to the NPF controller.

The PPF controller was originally proposed by Goh [16], and developed by Goh and Caughey [17] as an alternative to collocated direct velocity feedback. The PPF controller has the

following advantages: 1) the stability condition is non-dynamic; 2) it is not sensitive to spillover; 3) it is not destabilized by finite actuator dynamics; 4) it is amenable to a strain-based sensing approach. These advantages are experimentally validated by Fanson and Caughey [18]. In addition, it offers quick damping for a particular mode if the modal characteristics are well known. The PPF controller has been extensively used in flexible structure vibration control applications, such as in a programming structure by Dosch et al. [19], a thermally induced vibration by Friswell et al. [20], a slewing flexible frame by Leo and Inman [21], and a thin film rigidizable inflatable boom by Tarazaga et al. [22].

1.4. Piezoelectric Materials

Piezoelectricity is the property of certain materials that generate electricity when a stress is applied or vice versa. Piezoelectricity is in both mechanical and electrical domains and coupling between these domains exists. The direct piezoelectric effect is defined for the transduction of mechanical energy such as stress-strain to electrical energy namely electric field displacement. The reverse relation is called the inverse piezoelectric effect. The relation between these two domains is depicted in Figure 1-7.

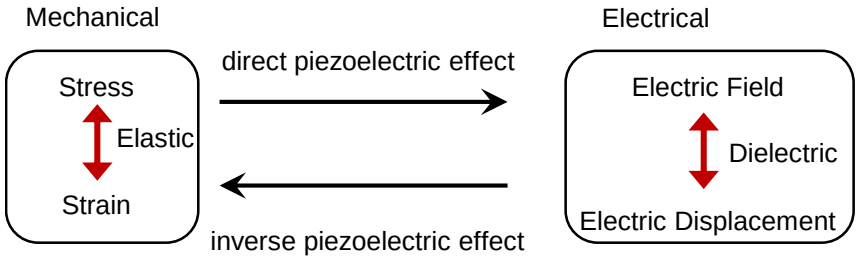

Figure 1-7: Physical domains and transduction in piezoelectric materials.

1.5. Mechanical Behavior

Figure 1-8 shows the three dimensional coordinates. In this double index notation $i, j =$ 1,2,3 of the coordinate system, the first digit indicates the surface number, and the second digit shows the direction.

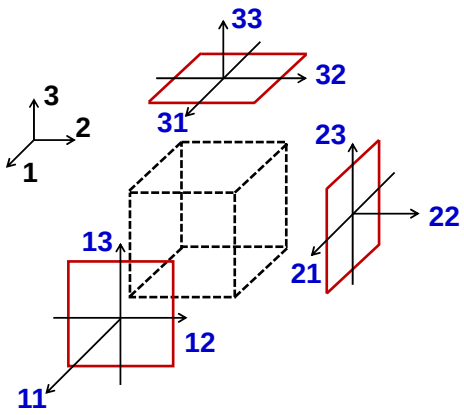

Figure 1-8 : Designation of the material axis and surfaces.

The displacement-strain relations can be written in tensor form as [23],

$$S_{ij} = \frac{1}{2}\left(\frac{\partial u_i}{\partial x_j} + \frac{\partial u_j}{\partial x_i}\right) \tag{1.5}$$

where S_{ij} shows the strain tensor, and u_i and u_j denote mechanical displacement.

Using the Cartesian coordinates, normal and shear stresses on the surface can be written as [24]

$$\tau_1 = T_{11}\tilde{x}_1 + T_{12}\tilde{x}_2 + T_{13}\tilde{x}_3 \tag{1.6}$$

$$\tau_2 = T_{21}\tilde{x}_1 + T_{22}\tilde{x}_2 + T_{23}\tilde{x}_3 \tag{1.7}$$

$$\tau_3 = T_{31}\tilde{x}_1 + T_{32}\tilde{x}_2 + T_{33}\tilde{x}_3 \tag{1.8}$$

where T_{ij} is the stress tensor. Using the symmetry property, the stress and strain have the form

$$T_{ij}=T_{ji} \tag{1.9}$$

$$S_{ij} = S_{ji} \tag{1.10}$$

The shear and normal stress vector [24] is constructed as

$$\boldsymbol{T} = \begin{bmatrix} T_{11} \\ T_{22} \\ T_{33} \\ T_{23} \\ T_{13} \\ T_{12} \end{bmatrix} \tag{1.11}$$

and the corresponding strain vector is given by

$$\boldsymbol{S} = \begin{bmatrix} S_{11} \\ S_{22} \\ S_{33} \\ 2S_{23} \\ 2S_{13} \\ \mathbf{2}S_{12} \end{bmatrix} \tag{1.12}$$

The contracted form of the stress vector is

$$\boldsymbol{T} = \begin{bmatrix} T_1 \\ T_2 \\ T_3 \\ T_4 \\ T_5 \\ T_6 \end{bmatrix} \tag{1.13}$$

and the contracted strain vector is

$$\boldsymbol{S} = \begin{bmatrix} S_1 \\ S_2 \\ S_3 \\ S_4 \\ S_5 \\ S_6 \end{bmatrix} = \begin{bmatrix} \frac{\partial}{\partial x_1} & 0 & 0 \\ 0 & \frac{\partial}{\partial x_2} & 0 \\ 0 & 0 & \frac{\partial}{\partial x_3} \\ 0 & \frac{\partial}{\partial x_3} & \frac{\partial}{\partial x_2} \\ \frac{\partial}{\partial x_3} & 0 & \frac{\partial}{\partial x_1} \\ \frac{\partial}{\partial x_2} & \frac{\partial}{\partial x_1} & 0 \end{bmatrix} \begin{bmatrix} u_1 \\ u_2 \\ u_3 \end{bmatrix} \tag{1.14}$$

The stress-strain relations for a linear elastic material can be shown as

$$\boldsymbol{S} = s\,\boldsymbol{T} \tag{1.15}$$

$$\boldsymbol{T} = c\,\boldsymbol{S} \tag{1.16}$$

where

$$c = s' \tag{1.17}$$

and s is the compliance matrix and is given by

$$s = \begin{bmatrix} s_{11} & s_{12} & s_{13} & s_{14} & s_{15} & s_{16} \\ s_{21} & s_{22} & s_{23} & s_{24} & s_{25} & s_{26} \\ s_{31} & s_{32} & s_{33} & s_{34} & s_{35} & s_{36} \\ s_{41} & s_{42} & s_{43} & s_{44} & s_{45} & s_{46} \\ s_{51} & s_{52} & s_{53} & s_{54} & s_{55} & s_{56} \\ s_{61} & s_{62} & s_{63} & s_{64} & s_{65} & s_{66} \end{bmatrix} \tag{1.18}$$

Assuming orthotropy and considering the symmetry property,

$$s = \begin{bmatrix} \frac{1}{Y_1} & -\frac{\upsilon_{12}}{Y_1} & -\frac{\upsilon_{13}}{Y_1} & 0 & 0 & 0 \\ -\frac{\upsilon_{21}}{Y_2} & \frac{1}{Y_2} & -\frac{\upsilon_{23}}{Y_2} & 0 & 0 & 0 \\ -\frac{\upsilon_{31}}{Y_3} & -\frac{\upsilon_{32}}{Y_3} & \frac{1}{Y_3} & 0 & 0 & 0 \\ 0 & 0 & 0 & \frac{1}{G_{23}} & 0 & 0 \\ 0 & 0 & 0 & 0 & \frac{1}{G_{13}} & 0 \\ 0 & 0 & 0 & 0 & 0 & \frac{1}{G_{12}} \end{bmatrix} \tag{1.19}$$

where Y_i is the elastic modulus, υ_{ij} is the Poisson ratio, and G_{ij} is the shear modulus. The moduli are related by:

$$\frac{\upsilon_{ij}}{Y_i} = \frac{\upsilon_{ji}}{Y_j} \tag{1.20}$$

and considering isotropic material, modulus and compliance matrices can be defined as

$$s = \frac{1}{Y}\begin{bmatrix} 1 & -\upsilon & -\upsilon & 0 & 0 & 0 \\ -\upsilon & 1 & -\upsilon & 0 & 0 & 0 \\ -\upsilon & -\upsilon & 1 & 0 & 0 & 0 \\ 0 & 0 & 0 & 2(1+\upsilon) & 0 & 0 \\ 0 & 0 & 0 & 0 & 2(1+\upsilon) & 0 \\ 0 & 0 & 0 & 0 & 0 & 2(1+\upsilon) \end{bmatrix} \tag{1.21}$$

and

$$c = \frac{Y}{(1+\upsilon)(1-2\upsilon)}\begin{bmatrix} (1-\upsilon) & 0 & 0 & 0 & 0 & 0 \\ 0 & (1-\upsilon) & 0 & 0 & 0 & 0 \\ 0 & 0 & (1-\upsilon) & 0 & 0 & 0 \\ 0 & 0 & 0 & (1-2\upsilon)/2 & 0 & 0 \\ 0 & 0 & 0 & 0 & (1-2\upsilon)/2 & 0 \\ 0 & 0 & 0 & 0 & 0 & (1-2\upsilon)/2 \end{bmatrix} \tag{1.22}$$

1.6. Electrical Behavior

The electrostatic property of a piezoelectric material is based on the Coulomb's Law, which defines the electric forces ($\vec{F}$) between the charges. Figure 1-9 illustrates the force between two charges.

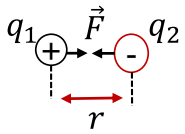

Figure 1-9: Electrostatic force ($\vec{F}$) between charges.

The electrostatic force between two charged particles, defined by Coulomb's law, is

$$\vec{F} = \frac{kq_1q_2}{r^2} \tag{1.23}$$

where q is charge, r is distance and k is

$$k = \frac{1}{4\pi\varepsilon_0} \tag{1.24}$$

where ε_0 is the permittivity of vacuum. The permittivity (ε) of the material is a measure of how much electric field is generated per unit charge. The electric field intensity ($\vec{E}$) produced by unit charge is the electric force per unit charge and is given by

$$\vec{E} = \frac{\vec{F}}{q} = \frac{kq}{r^2} \tag{1.25}$$

There is also a relation between the electric field intensity and the permittivity of the materials, shown as

$$\vec{E} = \frac{\sigma}{\varepsilon_0} \tag{1.26}$$

where σ is charge density.

The electric field induced (E) by an applied voltage (V) between electrodes is demonstrated in Figure 1-10.

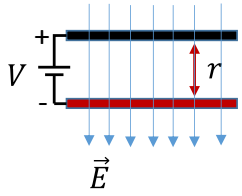

Figure 1-10: Electric field between the isolated electrodes.

Piezoelectric materials, showing the ferroelectric property, exhibit an electric displacement under the electric field. An inverse field induced in the opposite direction to the electric field intensity vector due to the shift of positive and negative charges in the dipole pairs. This field is called the polarization ($\vec{P}$) vector and is defined with a vector from negative to positive charges. Figure 1-11 demonstrates the effects of the electric field on ferroelectric materials.

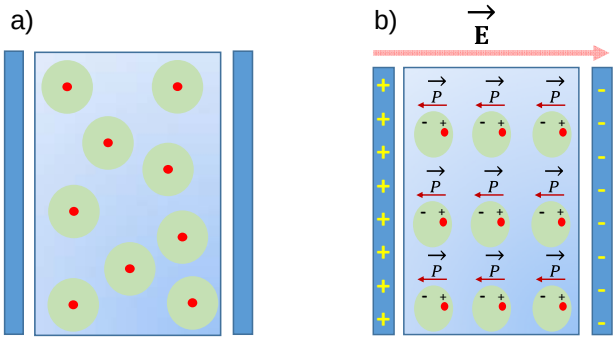

Figure 1-11: Representation of the electric field effect on dipoles a) without electric field, b) with electric field.

Total electric displacement noted by $\vec{D}$ is how electric field $\vec{E}$ influences the organization of electric charges in a given medium, including charge migration and electric dipole orientation. Total displacement [25] is given as

$$\vec{D} = \varepsilon\,\vec{E} = \varepsilon_0\vec{E} + \vec{P} = \varepsilon_0\vec{E} + \varepsilon_0\chi_e\vec{E} = \varepsilon_0(1+\chi_e)\vec{E} \tag{1.27}$$

The relative permittivity ε_r is defined by using the physical electron property χ_e, namely electron susceptibility. This physical measure varies when the material is changed and shows the electron behavior under the electric field.

Permittivity is given by:

$$\varepsilon_r = (1+\chi_e)\,,\ \vec{D} = \varepsilon_0\varepsilon_r\vec{E} \text{ and } \varepsilon = \varepsilon_0\varepsilon_r \tag{1.28}$$

The piezoelectric effect between the mechanical property stress (T) and electric displacement D can be defined as a proportional relationship [24]:

$$D = d\,T \tag{1.29}$$

where d is piezoelectric constant. The total mechanical and electrical system is represented by the so-called constitutive relationships given by [24]

$$\begin{bmatrix} S \\ D \end{bmatrix} = \begin{bmatrix} s & d \\ d & \varepsilon \end{bmatrix} \begin{bmatrix} T \\ E \end{bmatrix} \tag{1.30}$$

where the off-diagonal terms of Eq. (1.30) show the electromechanical coupling. In this equation, the resulting strain (S) and electrical displacement (D) and applied stress (T) and electric field (E) are showed. s and ε are directional constants and show the mechanical and electrical constitutive relations. An inverse relation can be written as [24]

$$\begin{bmatrix} T \\ E \end{bmatrix} = \begin{bmatrix} \frac{1}{s}\left(\frac{1}{1-d^2/s\varepsilon}\right) & -\frac{d/s\varepsilon}{1-d^2/s\varepsilon} \\ -\frac{d/s\varepsilon}{1-d^2/s\varepsilon} & \frac{1}{\varepsilon}\left(\frac{1}{1-d^2/s\varepsilon}\right) \end{bmatrix} \begin{bmatrix} S \\ D \end{bmatrix} \tag{1.31}$$

and can be rewritten as,

$$\begin{bmatrix} T \\ E \end{bmatrix} = \begin{bmatrix} \frac{1}{s}\frac{1}{1-k^2} & -\frac{1}{d}\frac{k^2}{1-k^2} \\ -\frac{1}{d}\frac{k^2}{1-k^2} & \frac{1}{\varepsilon}\frac{1}{1-k^2} \end{bmatrix} \begin{bmatrix} S \\ D \end{bmatrix} \tag{1.32}$$

where the piezoelectric coupling coefficient is

$$k = \frac{d}{\sqrt{s\varepsilon}} \tag{1.33}$$

The mechanical constants of a piezoelectric material can be determined by simplified constitutive relations under certain assumptions. For zero electric field ($E = 0$), constitutive equations become,

$$S = s\,T \tag{1.34}$$

$$D = d\,T \tag{1.35}$$

for zero electric displacement ($D = 0$) constitutive equations can be written as

$$S = s\,(1 - k^2)T \tag{1.36}$$

$$E = \frac{k^2}{d(1-k^2)}\mathrm{S} \tag{1.37}$$

The strain difference between two types of boundary conditions can be represented by the compliance relations,

$$s^D = s^E\,(1 - k^2) \tag{1.38}$$

1.7. The Macro-Fiber Composite Actuator

Figure 1-12 shows the structure of the MFC actuator. The MFC consists of PZT fibers, epoxy as adhesive, and two layers of electrodes. The PZT fibers are sandwiched between two electrode film layers using epoxy. A kapton insulation layer covers all surfaces.

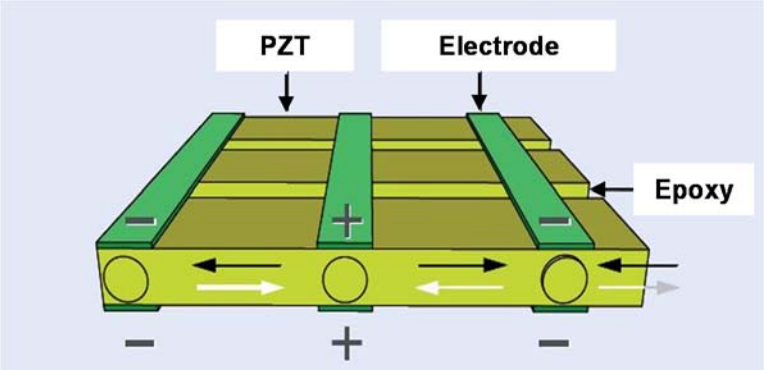

Figure 1-12: MFC actuator with components [26].

As shown in Figure 1-13, the electrodes are distributed in an interdigitated manner. This allows to create the electric field along the PZT fibers and induce in-plane poling. The MFC actuator can be bonded to composite structure surfaces and provide a bending moment.

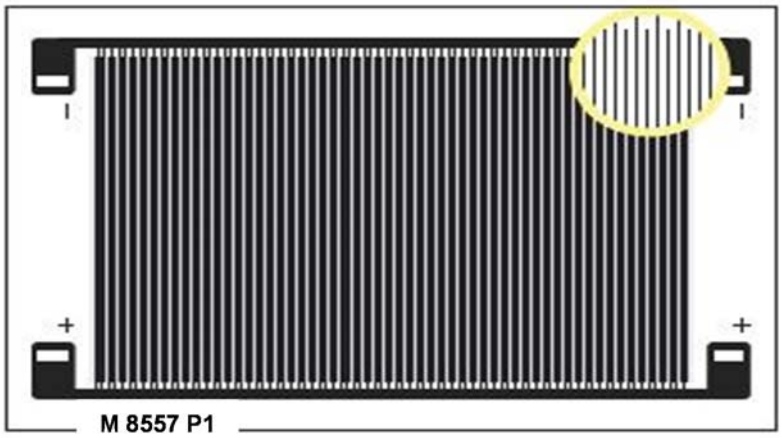

Figure 1-13: MFC actuator with electrode connection [27].

The actuation of a unimorph structure is done by using a unimorph Macro-Fiber Composite (MFC) device in the so-called *33* mode. When the electric field is applied to the patch it causes strain. Due to the offset between the actuator mid-plane and the neutral axes of the composite, the stress induced by the MFC creates a bending moment forcing the structure to bend. The stress created by the MFC actuator is assumed not to add any additional dynamics to the system based on the following relations.

$$M = d_{33} Y_3 (A\, r_a)(V(t)/\Delta_{el}) \tag{1.39}$$

$$M = C_m V(t) \tag{1.40}$$

where M is the bending moment generated by the piezoelectric devices. d_{33} is the piezoelectric coefficient showing the strain resulting from the unit electric field applied. The modulus of the structure is shown by Y_3, the geometric coupling terms are the area of MFC cross-section (A), and r_a is the moment arm between neutral axis and MFC mid-plane. Δ_{el} is the distance between the electrodes.

1.8. Research Goals and Objectives

The goal of this thesis is to show the feasibility of the hybrid controller as a strategy to achieve bidirectional state switch of bistable structures. The first objective is to show the theoretical closed loop behavior of the hybrid controller for its PPF and NPF components over a range of parameters. The second objective is to determine the theoretical energy and performance characteristic of the hybrid controller by varying the controller parameters. The third objective is to test the concept experimentally to determine stability and energy consumption.

1.9. Outline of the Thesis

Chapter 2 discusses the dynamic behavior of bistable structures and a linear model with and without the controller. In addition, the time and frequency response of the open loop and closed loop systems are examined. A stability algorithm used to determine the stability of the system from the time response is introduced and compared to the well-known Routh-Hurwitz method. After the comparison, the stability results for both components of the hybrid controller are presented and discussed. Based on the stability results, the parametric energy and performance characteristics of the controller are demonstrated.

Chapter 3 introduces the experimental setup and explains the procedures followed. Detailed information is provided for each component of the experiment such as structure, measurement devices, software to implement the controller, signal generation and the acquisition system. Also, the system identification methods and the controller implementation steps are

explained. The feasibility of the hybrid controller is demonstrated. Additionally, experimental parametric analysis is conducted, and a comparative discussion is presented.

Chapter 4 provides a summary of the results from this research. The publications stemming from the research are listed. A discussion of conclusions, recommendations and future work is also presented.

CHAPTER 2:
THEORETICAL DYNAMIC MODEL

2.1. Introduction

This chapter presents theoretical analysis of the hybrid controller using analytical and numerical simulation methods. First, in Section 2.2, the dynamic behavior of a bistable plate is discussed. A second-order linear model is developed for the equilibrium states of the bistable plate. Next, the hybrid controller is covered and the closed loop property of the controller is explained in Section 2.4 and 2.5. Finally, in Section 2.6 and Section 2.10 the stability and performance characteristics of the system are presented and discussed.

2.2. The Bistable Structure and Linearization near Equilibria

The dynamic behavior of a bistable structure is highly complex and may show chaotic oscillations. When the structure is oscillating from one stable equilibrium position to another, a jump phenomenon occurs at the unstable equilibrium that is highly nonlinear in nature. However, the dynamics around the equilibrium positions are less complex. For small perturbations around the equilibrium positions, the system dynamics show linear behavior. For this reason, a linear model can be used to cover two equilibrium states of a bistable structure.

The linearization process considers the structural inertia, stiffness, and internal non-conservative losses. A lumped stiffness is assumed for the overall structure including the actuator contribution. The structural losses are modeled by a linear viscous damping model.

The linearized model for each state of the bistable structure can be reduced to a lumped model of the system. Figure 2-1 shows an equivalent model of a bistable plate. The physical representation of the structure can be shown by the position proportional spring (k_1) and the velocity proportional damper (c_1). The inertial property of the structure is represented by the mass (m_1). The overall structure is modeled as a single degree-of-freedom (SDOF) system.

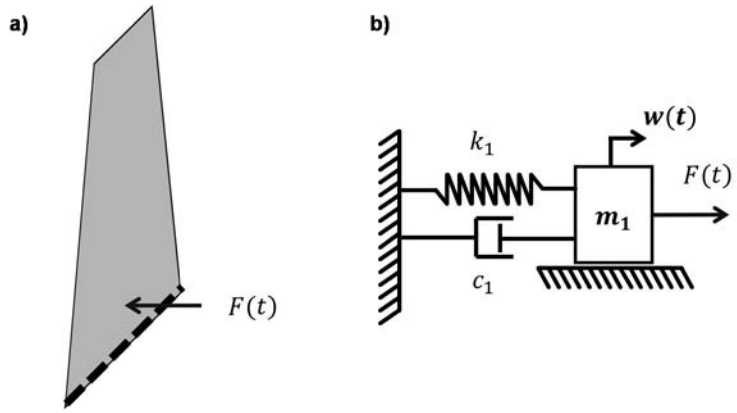

Figure 2-1: Bistable structure about equilibrium position, a) illustration, b) mechanical representation.

2.3. Physical Representation of the Coupled System

The mechanical analogy of the electrically realized controller is presented in Figure 2-2 to gain a better understanding of the hybrid controller. For the PPF controller, the reaction force to sensed displacement is equivalent to a spring in the mechanical domain. From Eq. (1), the energy dissipative term is only dependent on the response of the second degree-of-freedom; therefore, the mechanical viscous damping element is placed between the fixed reference and m_2. For this configuration, the second mass-damper system helps to dissipate the energy of the structure. However, when it comes to destabilization provided by the NPF controller, conventional passive mechanical elements such as a spring or a damper are not enough to create a mechanical representation. The challenge is that destabilization requires a force generated in the same direction as acceleration, as opposed to a force generated against the direction of acceleration. Therefore, a theoretical spring is introduced using a conventional spring with a diagonal arrow.

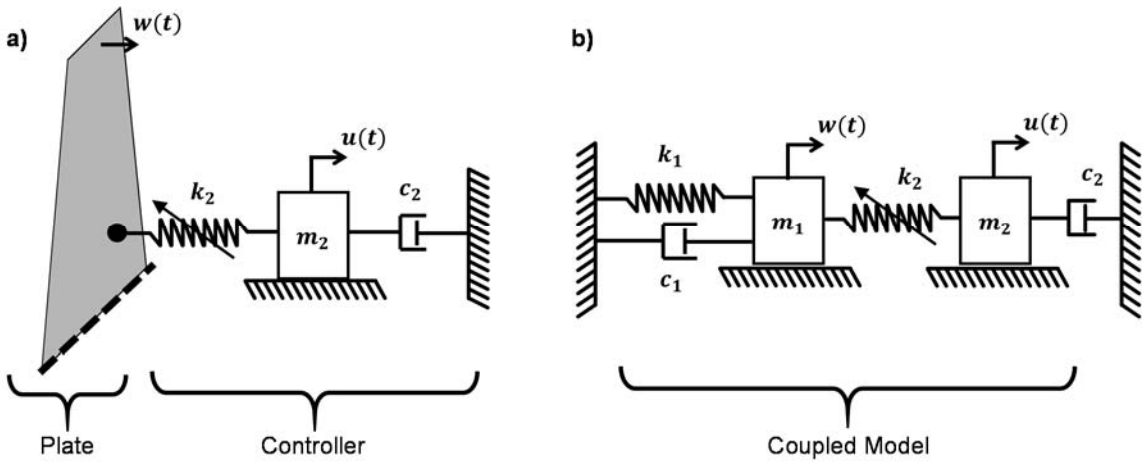

Figure 2-2: Representative models of the structure and the controller. a) Basic representation, and b) 2DOF coupled model.

2.4. Theoretical Time-Domain Response

Figure 2-3 shows the theoretical coupled and free time responses for the NPF and the PPF controller modes. The control efforts are presented for both cases. A saturation limit is set for the control voltage, which will be necessary in a physical implementation to protect the hardware.

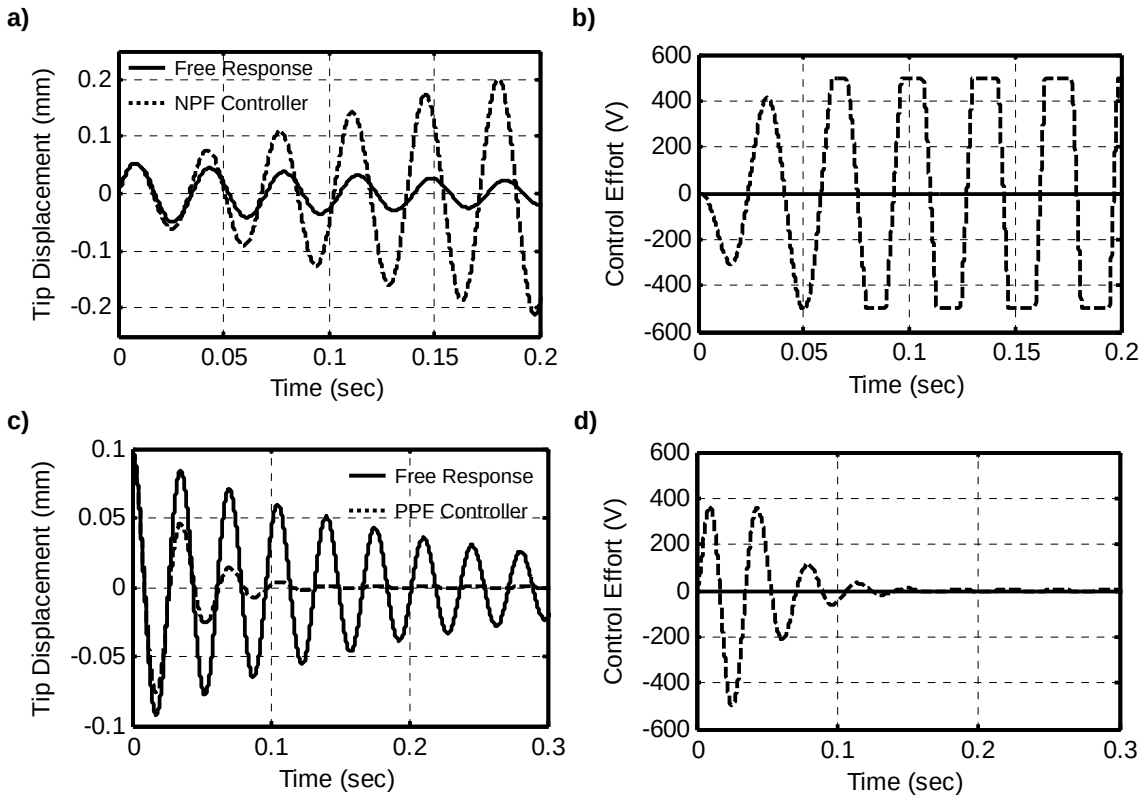

Figure 2-3: Time history of NPF a) tip displacement and b) control effort; PPF c) tip displacement and d) control effort.

It can be observed in Figure 2-3 (a) that the free response of the system decreases, while the controlled response increases exponentially with the application of the NPF controller. In Figure 2-3 (c), the PPF controller works in the opposite way to attenuate the displacement amplitude. As can be seen in Figure 2-3 (c), the closed-loop response decays much faster compared to the open-loop free response.

The control authority of the PPF controller highly depends on the gain. Figure 2-4 shows the closed loop time response for changing controller gain value. The tradeoff between the fast and oscillatory response should be noticed. When the gain is reduced, the apparent damping is reduced as well; hence, an oscillatory response occurs.

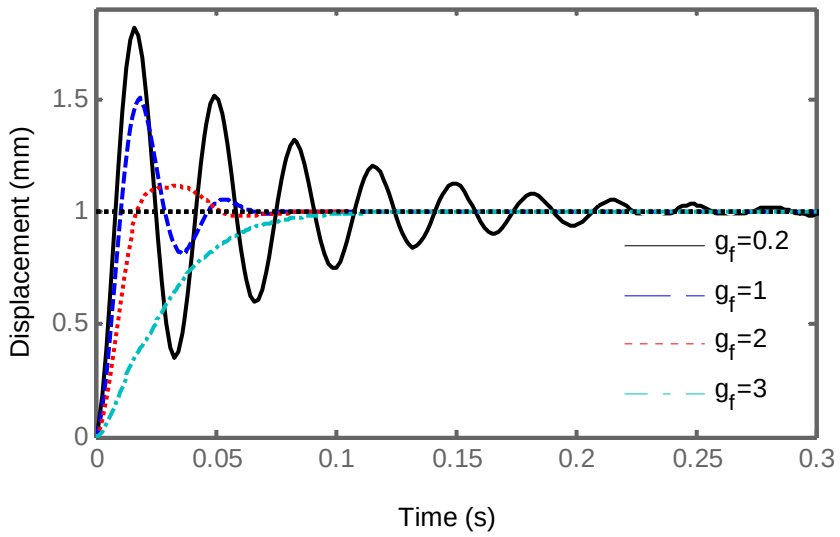

Figure 2-4: Step response of the PPF controller for varying controller gain.

The effect of the controller damping ratio on time response is presented in Figure 2-5. The suppression of the first peak value of the response is increasing as the damping ratio is increased. As can be seen in Figure 2-5, decay rate is increased when the damping ratio is increased up to the expected value of 0.707 ($\sqrt{2}/2$).

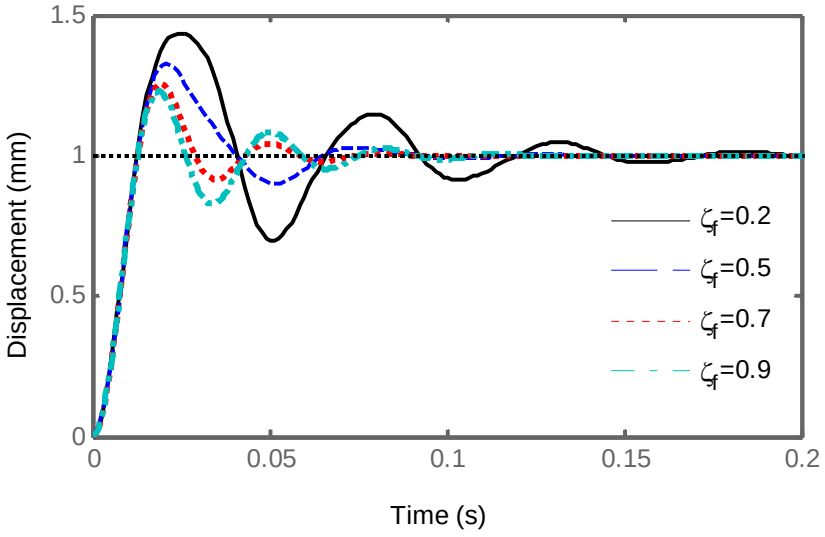

Figure 2-5: Step response of the PPF controller for varying damping ratios.

A numerical model for the hybrid controller is developed. The linear model of the controlled system is simulated using the numerical method of Dormand-Prince and the time responses for different parameter sets are presented in Figure 2-6 and Figure 2-7.

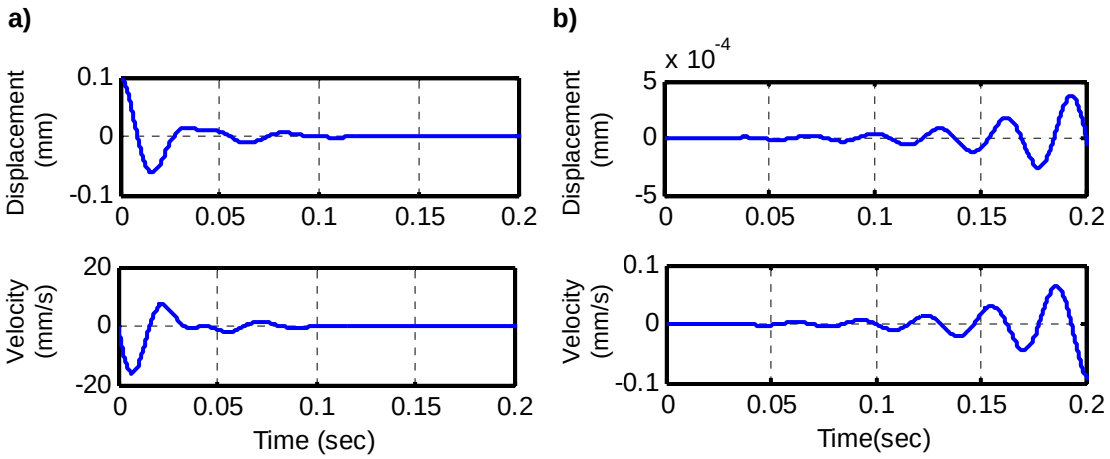

Figure 2-6: Numerical simulation time response for $\omega_r = 1.15$, $\zeta_f = 0.3$ and $g_f = 0.2$ a) PPF, b) NPF.

Figure 2-7 shows the time response for the hybrid controller strategy for a gain value of 0.2. This kind of response is acceptable; however, a small variation in the structural properties can make the controller behavior undesirable.

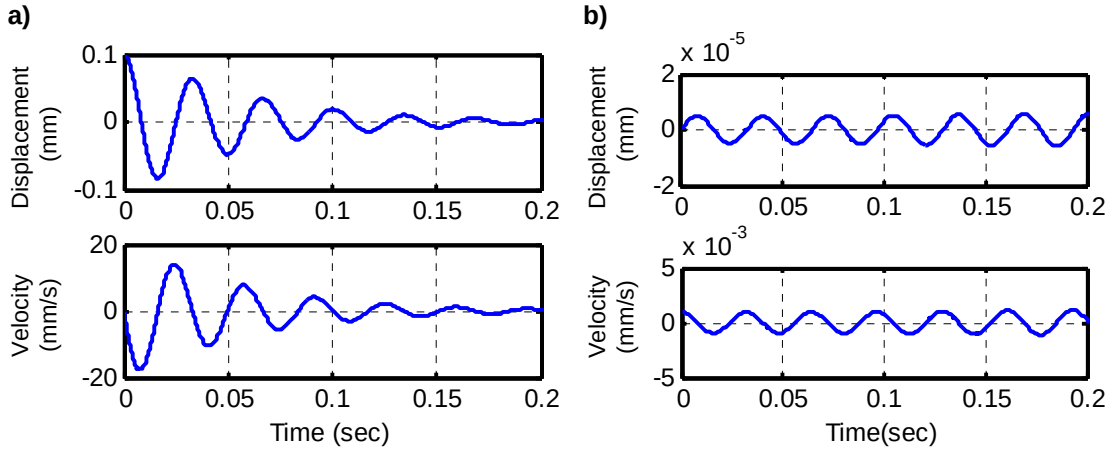

Figure 2-7: Numerical time response for $\omega_r = 1.15$, $\zeta_f = 0.3$ and $g_f = 0.1$, a) PPF, b) NPF.

2.5. Theoretical Frequency-Domain Response

The characteristics of the PPF and NPF controllers shown in Figure 2-8 are useful to explain how it manipulates the given input. Both controllers are showing second-order low-pass filter characteristics. The phase of the PPF is starting at zero at pre-resonance and switches to 180 degrees for post-resonance frequencies. The NPF controller has a negative 180 degrees phase for pre-resonance frequencies and zero phase for post-resonance frequencies.

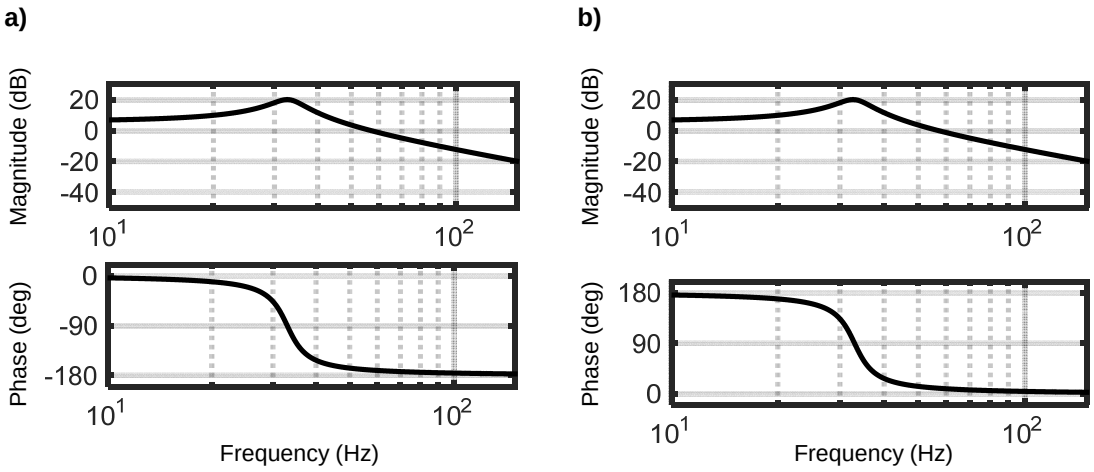

Figure 2-8: Examples of the frequency responses of the a) PPF and b) NPF controllers with $\omega_f = 33$, $\zeta_f = 0.1$ and $g_f = 2$.

The root-loci shown in Figure 2-9 demonstrates the general stability behavior of both controllers. The open loop poles of the controlled structure are shown using the "x" mark, and the closed loop poles are indicated by the "square" mark on the migration path for a specific gain value. The PPF controller gain paths are moving from the poles toward the zeroes at infinity towards the left-hand-plane (LHP) direction. This creates a stable gain range. Having a small migration path in the LHP, the NPF controller also has a small stable gain range. The NPF easily becomes unstable for values higher than the stable gain limit.

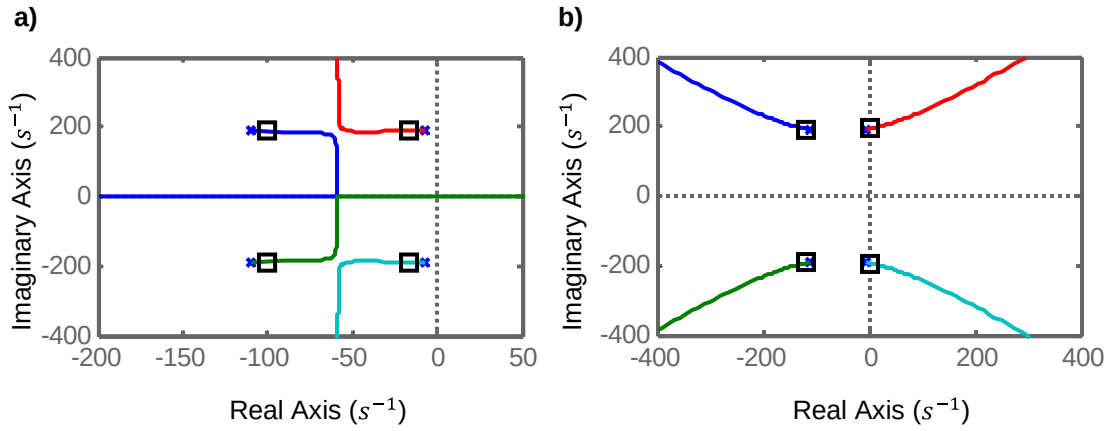

Figure 2-9: Root-loci for the two controllers with $\omega_f = 35$, $\zeta_f = 0.5$ a) PPF with $g_f = 0.5$, b) NPF with $g_f = 0.25$.

Figure 2-10 shows the effect of the controller damping ratio on a system with closed loop response using Nyquist plots for the PPF controller. The red "+" sign shows -1 on the real axis which is the critical point for indicating system stability. If a net encirclement around -1 occurs, the system is unstable.

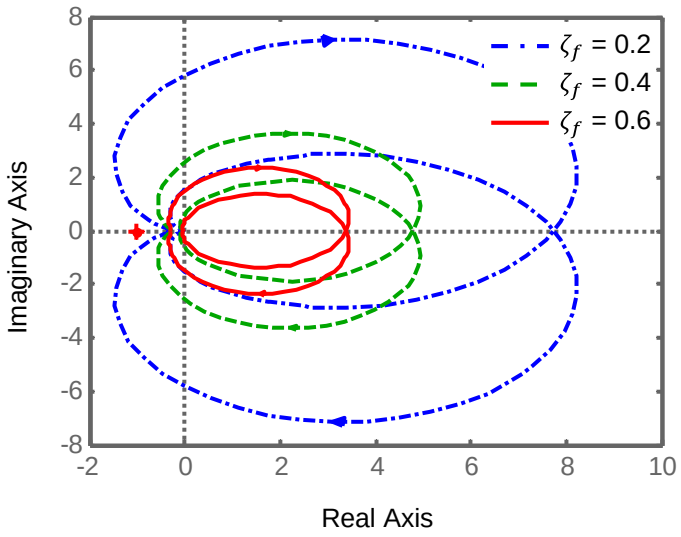

Figure 2-10: Closed-Loop Nyquist diagram for the PPF controller with varying damping ratio at $\omega_r = 1.15$ and $g_f = 1$.

Although the damping ratio of the controllers is decreased, the nominal closed-loop stability is not changed. However, the system loses its robustness for low damping ratios.

The closed-loop response of the NPF controller has a migration path from the poles to RHP. The NPF controller stability is not controller independent like the PPF controller. Damping augmentation from the controller is important for system stability and dynamic response. As can be seen in Figure 2-11, increasing damping results in a stable response which is not desired for the NPF mode.

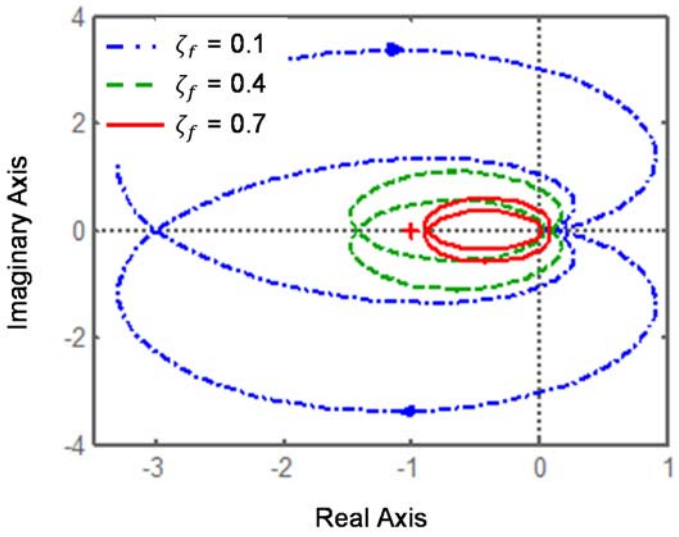

Figure 2-11: Closed-Loop Nyquist diagram for the NPF controller with varying damping at $\omega_r = 1.15$ and $g_f = 0.3$.

The controller frequency is also important for the closed-loop response. Instability can be achieved with a very low controller gain where the system is near resonance. However, the controller authority is weakened when the frequency is very low or high compared to the natural frequency of the system. This behavior can be seen in Figure 2-12.

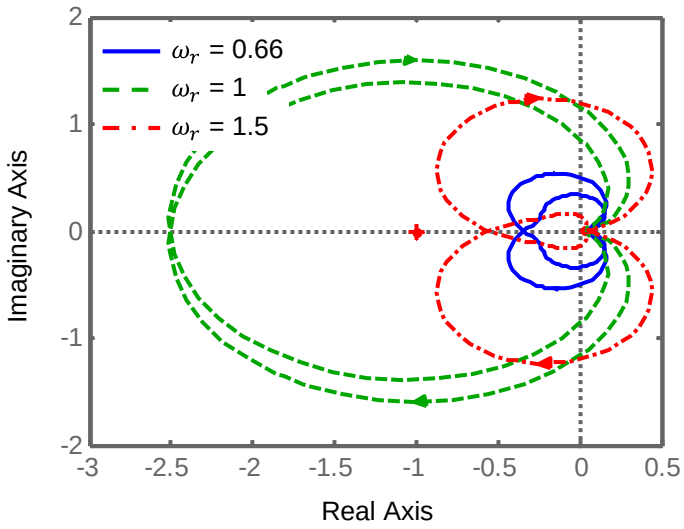

Figure 2-12: Closed-Loop Nyquist diagram for the NPF Controller with varying frequency ratio for $\zeta_f = 0.15$ and $g_f = 0.2$.

A frequency ratio sufficiently lower or higher than one results in a stable response where the unstable response is expected from the NPF controller. However, when the controller

produces an excitation input near the natural frequency of system, the force applied to the structures creates accumulation of system kinetic energy. This yields an unstable response, where the Nyquist diagram shows net encirclement around -1.

2.6. Parametric Stability Analysis

Stability is critical in understanding the PPF and the NPF controllers, the main components of the proposed hybrid controller. Motion is created using the NPF controller (unstable), and suppression is achieved using the PPF controller (stable). A parametric stability analysis is conducted to show the set of parameters leading to desirable and undesirable behavior.

2.7. Time-Domain Method

An algorithm is developed to determine the system behavior from the time response of the simulations. A three-parameter analysis is carried out and the results are later verified using the Routh-Hurwitz method.

First, a settling band is set, and the system entrance to this band is searched in the time history. All band crossovers are recorded. The time differences between the consequent crossovers are calculated. Then the system's natural period and the crossover interval are compared. The system is considered desirable (i.e. stable for PPF mode) if the crossover interval is less than 1.5 times the period of oscillation. The flow chart of the algorithm and a generic impulse response of the PPF controller are shown in Figure 2-13.

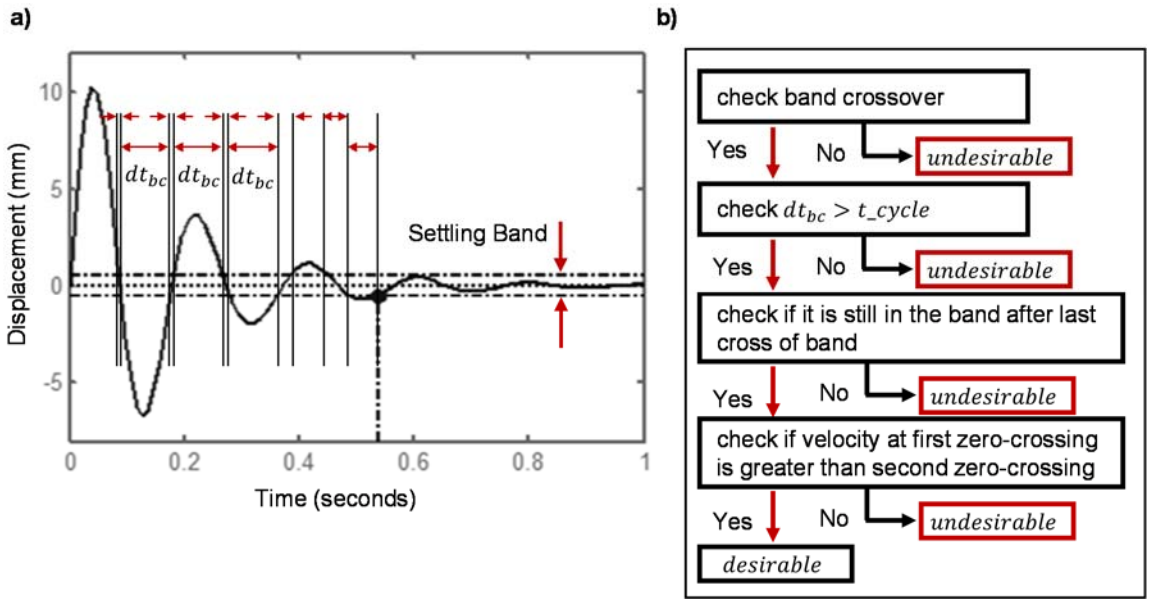

Figure 2-13: PPF controller, a) generic impulse response, b) stability algorithm flow chart.

The NPF algorithm detects the unstable time response by searching a threshold limit value that, in our application, is the unstable equilibrium. The initial condition of the system in this case is a small velocity disturbance. The NPF algorithm starts with a short simulation time due to the potentially large dynamic range of the response. When the instability pattern is observed, the time-domain simulation is repeated in a while loop until the response reaches the threshold limit. The NPF algorithm is presented in Figure 2-14.

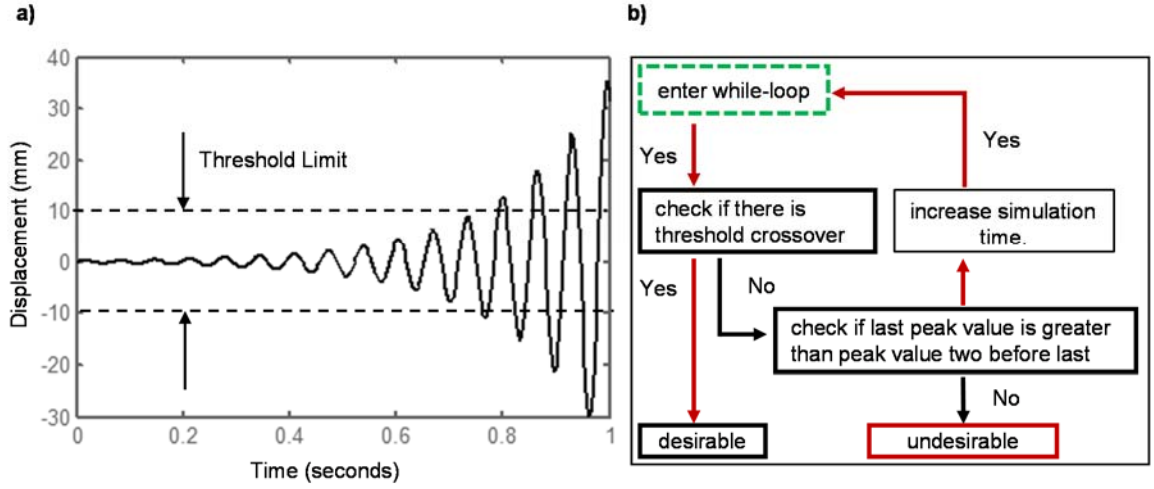

Figure 2-14: NPF controller, a) generic impulse response, b) stability algorithm flow chart.

2.8. Analytical Routh-Hurwitz Method

To determine stability, the well-known Routh-Hurwitz stability criteria are utilized. The criteria are based on the characteristic equation of the closed loop system. For a given characteristic equation,

$$a_0\lambda^n + a_1\lambda^{n-1} + a_2\lambda^{n-2} \ldots . a_{n-2}\lambda^2 + a_{n-1}\lambda^1 + a_n = 0 \tag{2.1}$$

a Hurwitz matrix is created from the coefficient of the equation as

$$\begin{bmatrix} a_1 & a_0 & 0 & 0 & 0 & 0 & & 0 \\ a_3 & a_2 & a_1 & a_0 & 0 & 0 & \cdots & 0 \\ a_5 & a_4 & a_3 & a_2 & a_1 & a_0 & & 0 \\ & & & \vdots & & & \ddots & \vdots \\ 0 & 0 & 0 & 0 & 0 & 0 & \cdots & a_n \end{bmatrix} \tag{2.2}$$

where the principle minors can be calculated as

$$\Delta_1 = a_1 \tag{2.3}$$

$$\Delta_2 = \begin{vmatrix} a_1 & a_0 \\ a_3 & a_2 \end{vmatrix} \tag{2.4}$$

$$\Delta_3 = \begin{vmatrix} a_1 & a_0 & 0 \\ a_3 & a_2 & a_1 \\ a_5 & a_4 & a_3 \end{vmatrix} \tag{2.5}$$

$$\Delta_n = \begin{vmatrix} a_1 & a_0 & 0 & \vdots & 0 \\ a_3 & a_2 & a_1 & \vdots & 0 \\ a_5 & a_4 & a_3 & \vdots & 0 \\ \cdots & \cdots & \cdots & \vdots & 0 \\ 0 & 0 & 0 & \vdots & a_n \end{vmatrix} \tag{2.6}$$

For the Hurwitz matrix and calculated principle minors, the system is stable if-and-only-if (iff) all the principle minors are greater than zero. For the system with PPF controller, the closed loop transfer function is determined using the transfer functions in (1.1) and (1.2).

$$\begin{aligned} s^4 + \left(B_n + B_f\right) s^3 + \left(B_n B_f + {w_n}^2 + {w_f}^2\right)s^2 + \left(B_n {w_f}^2 + B_f {w_n}^2\right)\mathrm{s} \\ + {w_n}^2 {w_f}^2\left(1 - g_n g_f\right) = 0 \end{aligned} \tag{2.7}$$

where $B_n = 2\zeta\omega_n$ and $B_f = 2\zeta_f\omega_f$. Using the coefficients of the characteristic equation, the Hurwitz matrix is

$$\begin{bmatrix} (B_n + B_f) & 1 & 0 & \cdots \\ (B_n {w_f}^2 + B_f {w_n}^2) & (B_n B_f + {w_n}^2 + {w_f}^2) & (B_n B_f + {w_n}^2 + {w_f}^2) & \cdots \\ 0 & {w_n}^2 {w_f}^2 (1 - g_f g_n) & (B_n {w_f}^2 + B_f {w_n}^2) & \cdots \\ 0 & 0 & 0 & \cdots \end{bmatrix}$$

$$\begin{bmatrix} \cdots & 0 & 0 & 0 \\ \cdots & 1 & 0 & 0 \\ \cdots & (B_n B_f + {w_n}^2 + {w_f}^2) & (B_n + B_f) & 1 \\ \cdots & 0 & 0 & {w_n}^2 {w_f}^2 (1 - g_n\, g_f) \end{bmatrix} \tag{2.8}$$

The principle minors of the controller are

$$\Delta_1 = (B_n + B_f) \tag{2.9}$$

$$\Delta_2 = B_n {w_f}^2 + B_f {w_n}^2 + B_n B_f (B_n + B_f) \tag{2.10}$$

$$\begin{aligned} \Delta_3 = B_n B_f \left[({w_n}^2 - {w_f}^2)^2 + (B_n + B_f)(B_n {w_f}^2 + B_f {w_n}^2) \right] \\ + g_f g_n (B_n + B_f)^2 {w_n}^2 {w_f}^2 \end{aligned} \tag{2.11}$$

$$\Delta_4 = {w_n}^2 {w_f}^2 (1 - g_n\, g_f)\, \Delta_3 \tag{2.12}$$

$\Delta_1, \Delta_2, \Delta_3$ are unconditionally greater than zero. However, Δ_4 is less than zero when $g_n\, g_f$ is greater than one. Also, one should note that stability is not dependent on dynamics of the controller and the structure.

For the NPF controller, the characteristic equation is slightly different:

$$\begin{aligned} s^4 + (B_n + B_f)\, s^3 + (B_n B_f + {w_n}^2 + {w_f}^2) s^2 + (B_n {w_f}^2 + B_f {w_n}^2) \mathrm{s} \\ + {w_n}^2 {w_f}^2 (1 + g_n g_f) = 0 \end{aligned} \tag{2.13}$$

The Hurwitz matrix is

$$\begin{bmatrix} (B_n + B_f) & 1 & 0 & \cdots \\ (B_n {w_f}^2 + B_f {w_n}^2) & (B_n B_f + {w_n}^2 + {w_f}^2) & (B_n B_f + {w_n}^2 + {w_f}^2) & \cdots \\ 0 & {w_n}^2 {w_f}^2 (1 + g_f g_n) & (B_n {w_f}^2 + B_f {w_n}^2) & \cdots \\ 0 & 0 & 0 & \cdots \end{bmatrix}$$

$$\begin{bmatrix} . & . & . & 0 & 0 & 0 \\ . & . & . & 1 & 0 & 0 \\ . & . & . & (B_n B_f + {w_n}^2 + {w_f}^2) & (B_n + B_f) & 1 \\ . & . & . & 0 & 0 & {w_n}^2 {w_f}^2 (1 + g_n\, g_f) \end{bmatrix} \tag{2.14}$$

The principle minors are

$$\Delta_1 = (B_n + B_f) \tag{2.15}$$

$$\Delta_2 = B_n {w_f}^2 + B_f {w_n}^2 + B_n B_f (B_n + B_f) \tag{2.16}$$

$$\Delta_3 = B_n B_f \left[({w_n}^2 - {w_f}^2)^2 + (B_n + B_f)(B_n {w_f}^2 + B_f {w_n}^2) \right] - g_f g_n (B_n + B_f)^2 {w_n}^2 {w_f}^2 \tag{2.17}$$

$$\Delta_4 = {w_n}^2 {w_f}^2 (1 + g_n\, g_f)\, \Delta_3 \tag{2.18}$$

Stability in this case is independent on system dynamics, since the principle minors of the Hurwitz matrix are not all unconditionally positive. The Δ_1 and Δ_2 are unconditionally positive; however, the sign of Δ_3 *and* Δ_4 depend on every parameter in the structure and controller.

For each parameter set, the results of the algorithm based on time history and the Routh-Hurwitz criteria are compared and presented in Figure 2-15 and Figure 2-16. The controller frequency is normalized with the system natural frequency, and this metric is given by $\omega_r = \omega_f / \omega_n$. It should be noted that a finite number of damping ratios and frequency ratios at discrete gain levels are evaluated; the stability is continuous otherwise. Figure 2-15 presents the comparison for the NPF controller.

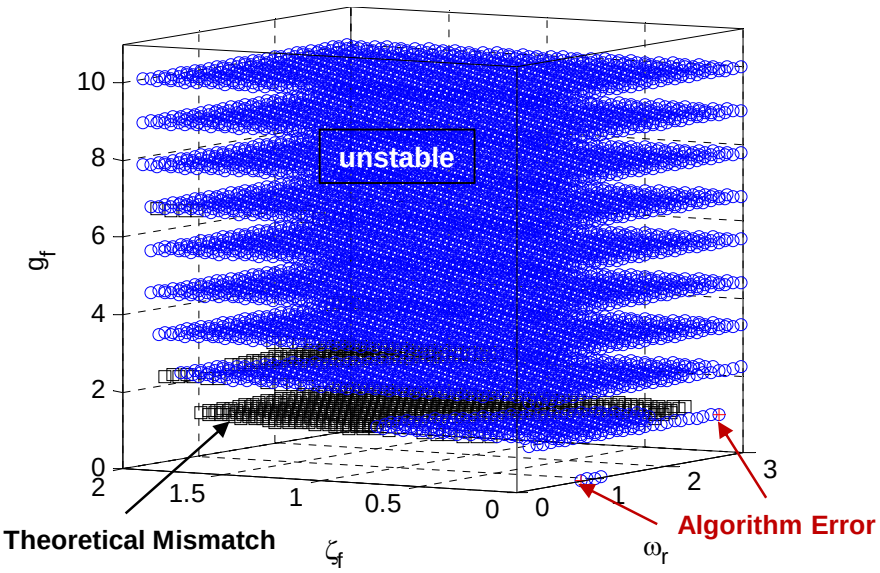

Figure 2-15: Comparison of the algorithm and the Routh-Hurwitz method for the NPF controller.

In Figure 2-15, the results from both methods are the same except for some parameters for low gain and high damping values. In these regions, while the Routh-Hurwitz criteria indicate a stable response, the numerical simulation gives an unstable response. There are only two points where the algorithm and the Routh-Hurwitz criteria conflict. These points are indicated in Figure 2-15 as a blue circle with a red "+" mark inside. The discrepancies at these points are due to the inherent stability issues of numerical integration methods. Figure 2-16 shows the comparison of the time-domain based algorithm and Routh-Hurwitz criteria for the PPF controller.

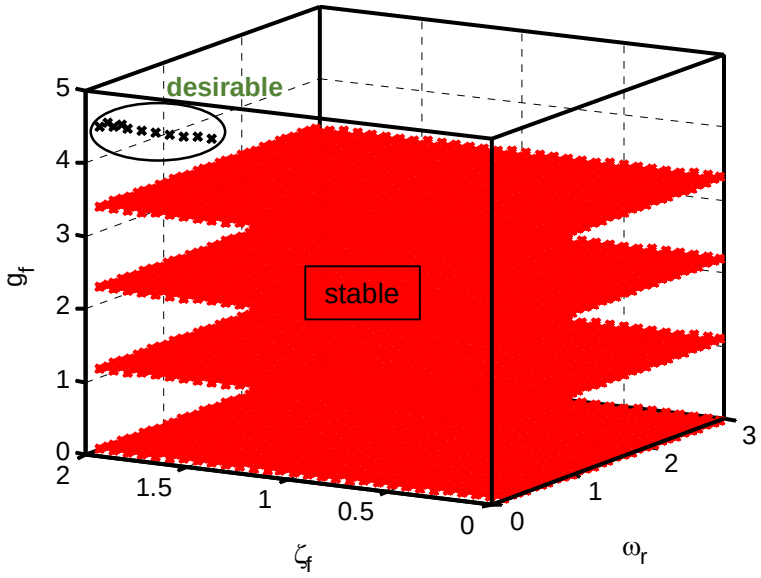

Figure 2-16: Comparison of the algorithm and the Routh-Hurwitz method for the PPF controller.

For the PPF controller, both methods match exactly and are highlighted with a red region. There are additional regions showing desirable points mentioned previously. These points show the stable-unstable time response character that can be used in the PPF mode and is considered desirable.

The stability of the hybrid controller in its PPF and NPF modes is presented in Figure 2-17 . The blue circles show the parameters causing an unstable NPF controller, where the red stars indicate parameters causing a stable PPF controller. The region created by the intersection of the parameters results in the desirable behavior of both controllers, resulting in a desirable hybrid controller response. These shared parameters are considered for a simple hybrid controller design since it fulfills the desirable characteristics of both controllers. A simple sign change enabled by a switch (as shown in Figure 1-4 and demonstrated in Figure 2-3) achieves the desired function of the proposed hybrid controller.

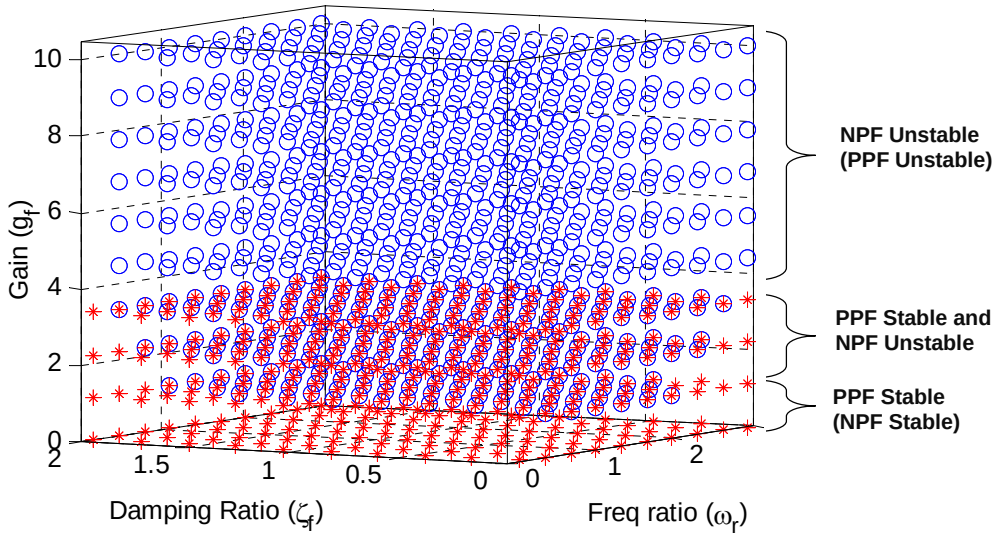

Figure 2-17: Three-parameter stability plot of the PPF and the NPF controllers and the intersection volume.

It is noted that the PPF and NPF parts of the hybrid controller can have different parameters and still achieve the desired function as a collective hybrid control scheme. Such additional flexibility in controller parameters may lead to a more efficient control strategy. This is the subject of future research.

2.9. Robustness of the HPF Controller

In addition to the nominal stability analysis, the stability margins for changing controller gain are studied. The bode diagrams of the closed-loop system in the PPF and NPF modes showing gain and phase margins are presented in Figure 2-18.

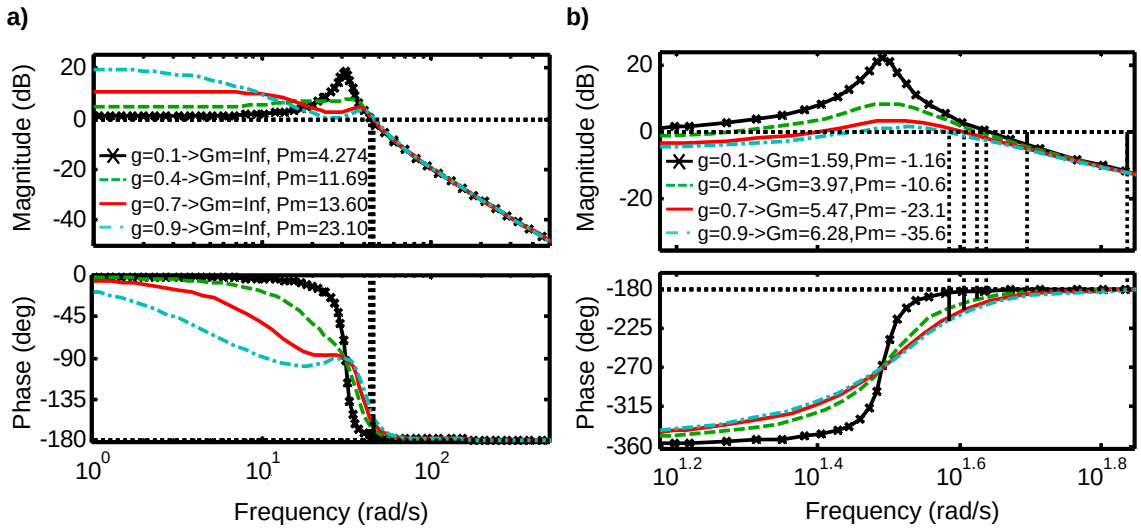

Figure 2-18: Stability margins of the a) PPF, b) NPF controller modes. Bode diagram magnitude and phase for $\omega_r = 1$ and $\zeta_f = 0.5$

As represented in Figure 2-18 (a), the phase margin of the PPF controller increases by increasing the controller gain. A large phase margin, achieved by increasing the gain, guarantees stability; hence the change in the phase caused by modeling and measurement errors will not destabilize the system. Also the gain margin of infinity shows that stability is secured even if other dynamical parameters such as controller frequency and damping ratio have large variances for the given gain values. The effect of gain on stability can be observed for the NPF controller mode in Figure 2-18 (b). By increasing the gain, the phase margin decreases and the gain margin increases. This indicates that the unstable characteristic of the NPF controller is guaranteed for high gain values.

2.10. Energy and Settling Time

It is also important to investigate energy consumption of the controller to perform a transition from one equilibrium position to the other. The hybrid controller has two types of energy transfer. The first one is to increase the amplitude of the oscillation around an equilibrium position using the NPF mode. Once the structure reaches the unstable equilibrium, there is no need for actuation. However, the potential (and kinetic) energy stored to overcome the unstable

equilibrium will cause unnecessary oscillations around the other stable equilibrium. This needs to be damped using the PPF mode of the hybrid controller.

The energy transfer for actuation and suppression is calculated separately by integration of the product of force and velocity along time using the following formula

$$E = \int_0^T F(t)\, V(t)\, dt. \tag{2.19}$$

In the NPF controller mode, the integration time is determined using the period from zero displacement to the time it takes to reach the unstable equilibrium. For the PPF mode, five-percent settling time is the integration time. The energy transfer of the system is presented in 3-D plots as shown in Figure 2-19 and Figure 2-21. The energy level is demonstrated by color ranging from blue to red.

Figure 2-19 presents energy transfer of the PPF controller until the structure enters 5% of the settling band for varying controller parameters. The energy values are normalized by the static energy. The color mapping ranges from red to blue indicating high to low energy and is used to visualize energy levels.

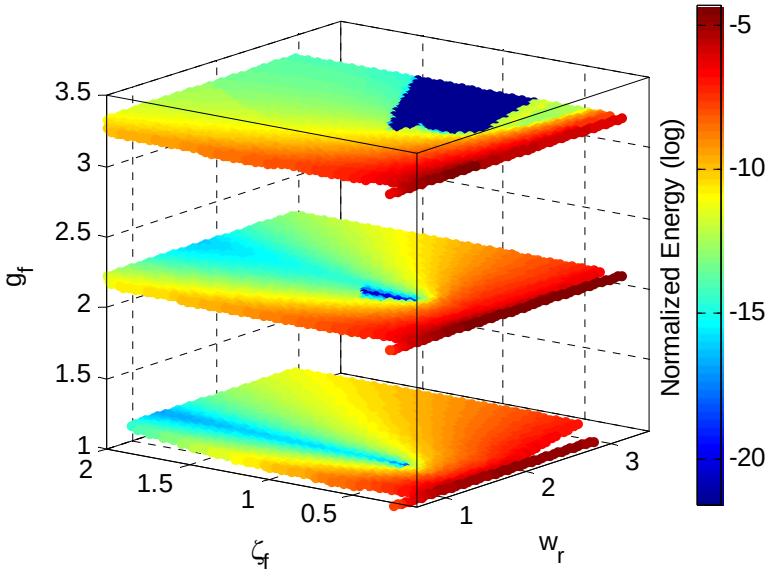

Figure 2-19: PPF controller energy consumption for suppression of the oscillation.

The variation of controller parameters shows a low and high energy region in Figure 2-19. First, the system response achieves band entrance with less energy transfer if the controller frequency is around the structure's natural frequency. This behavior is obvious in Figure 2-19

where the blue energy strip occurs around the frequency ratio of 1. For minimum energy suppression, a frequency ratio of 1, damping ratio of 0.707 and a controller gain of 2 is suggested.

Figure 2-20 presents the settling time it takes from initial disturbance to settling band entrance for the system with the PPF controller.

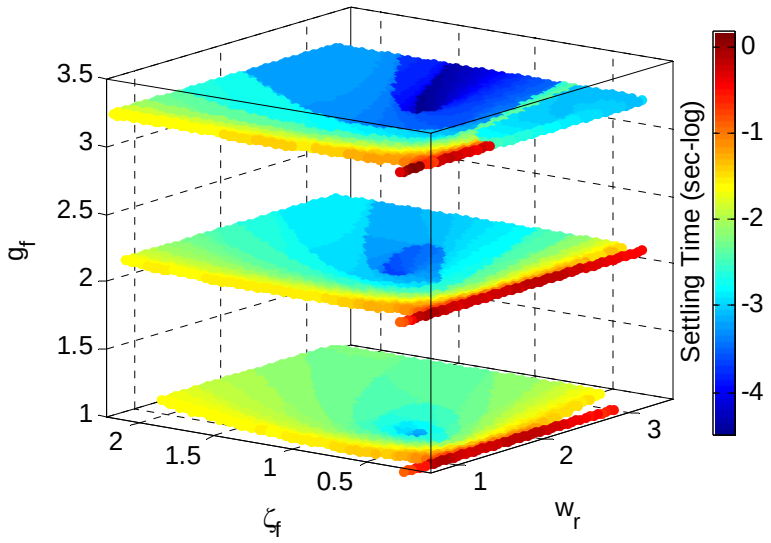

Figure 2-20: PPF controller settling time as controller performance.

The response enters the settling band faster when the controller gain is high. It can be noticed in Figure 2-20 that the increase in frequency ratio may yield a settling time if damping and gain are increased. For a fast controller response, a frequency ratio of 1, controller gain of 2 and damping ratio of 0.707 is suggested.

Figure 2-21 presents the NPF controller energy transfer required to destabilize a structure from a stable position to an unstable equilibrium threshold value.

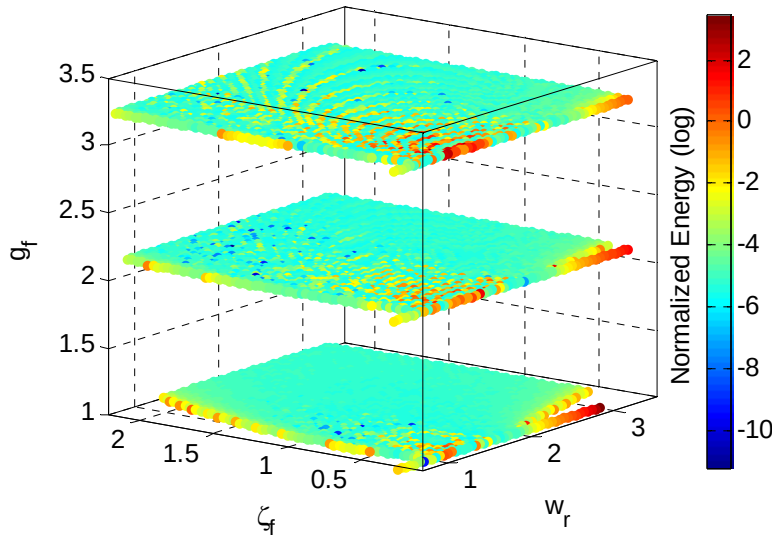

Figure 2-21: NPF controller energy consumption to reach a threshold value.

The energy consumption to achieve snap-through does not vary much by the change in parameters. However, an interesting pattern appears around a frequency ratio of 1.

Figure 2-22 presents the settling time it takes from an initial disturbance to reach the unstable equilibrium threshold value under the NPF controller.

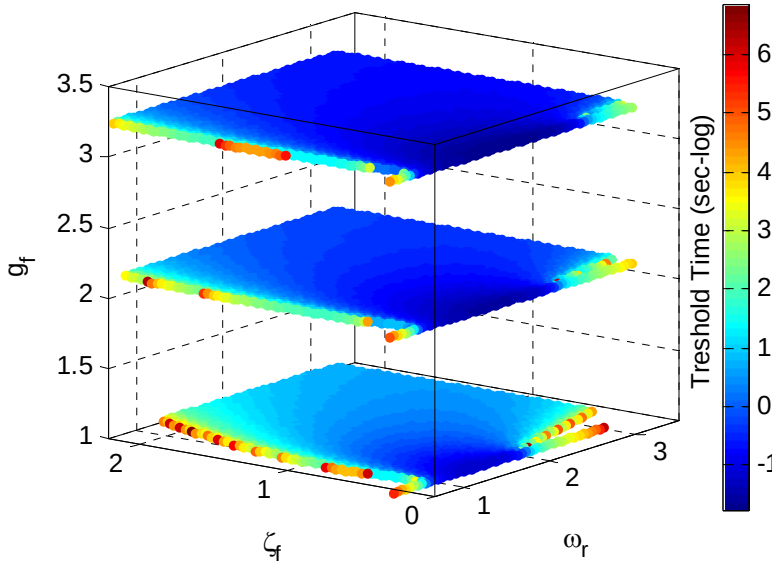

Figure 2-22: NPF controller threshold time.

A pattern of wide diagonal low threshold time regions is observed in the direction of high damping and increasing frequency ratio. Furthermore, the energy lines in the energy response show up as high values in the threshold time plot.

2.11. Conclusions

This chapter presented the assumptions to model bistability and the dynamic behavior of the linear model. Next, the closed-loop behavior of the model with proposed hybrid position controller is discussed. Algorithms to determine stability from the time response are introduced and the stability results for the PPF and NPF modes are presented. Finally, parametric energy and performance characteristics of the controller are discussed.

Table 2-1 shows the suggested parameters for performance metrics such as the desired stability, energy and time.

Table 2-1: Conclusions based on the idealized theoretical models.

	PPF			**NPF**		
	ω_r	ζ_f	g_f	ω_r	ζ_f	g_f
Stability	any	any	< 3.5	$f(\zeta_f, g_f)$	$f(\omega_r, g_f)$	> 3.5
Lowest Energy	~1	$0.5 - 0.8$	~2	> 1	> 0.707	< 1
Shortest Time	~1	$0.5 - 0.8$	~3.5	1	< 0.707	> 2

For stability of the PPF controller, the controller gain should be selected less than 3.5, and the other parameters can be selected in a wide range. For the NPF controller, a gain greater than 3.5 guarantees the unstable characteristic. For a gain value lower than 3.5, other parameters must be selected appropriately to achieve desired stability.

The lowest energy for the PPF controller mode can be achieved when the frequency ratio is around 1, damping ratio is between 0.5 and 0.8, and controller gain is around 2. For the NPF controller, frequency ratio must be greater than 1, damping ratio greater than 0.707, and the controller gain less than 1.

For the shortest response time, the frequency ratio of 1, damping ratio between 0.5 and 0.8, and controller gain around 3.5 is suggested for PPF controller. For the NPF controller, natural frequency of 1, damping ratio less than 0.707, and controller gain greater than 2 can be utilized.

CHAPTER 3:
EXPERIMENTAL ANALYSIS AND COMPARISON

3.1. Introduction

In this chapter, experimental analysis including experimental procedures, feasibility tests of the hybrid controller, stability and energy analyses are presented. First, the experimental setup is introduced. The structural properties of a composite plate used as a bistable structure are explained. Next, the equipment, measurement devices, control board, and the software are introduced. A detailed signal flow diagram is presented to explain the interaction between the experimental components. Next, system identification tests are carried out both to determine the structural parameters, and to show the linear property of the structure around stable equilibria. Once the structure parameters are determined, the feasibility tests of the HPF controller are performed, and the results are discussed. Next, parametric stability experiments are conducted to determine system behavior in real-life conditions, and results are compared to the theoretical analysis. Additionally, parametric energy analysis of the HPF controller is performed based on the experimental time response data, and similarity to theoretical results is discussed.

3.2. Experimental Setup

The experiment consists of two parts: the structure with the actuators and the signal acquisition-generation-processing system. For the structure, a low aspect ratio unsymmetric cross-ply laminated bistable composite plate is used by [28]. The plate has a 0.73 taper ratio with 139 mm tip chord, 254 mm root chord and a span of 290 mm. For the excitation, two M8557-P1 type Macro Fiber Composite (MFC) actuators are bonded near the clamp. The MFCs are operating in the *33* mode of actuation which provides higher actuation authority compared to the *31* mode. The specimen is shown in Figure 3-1.

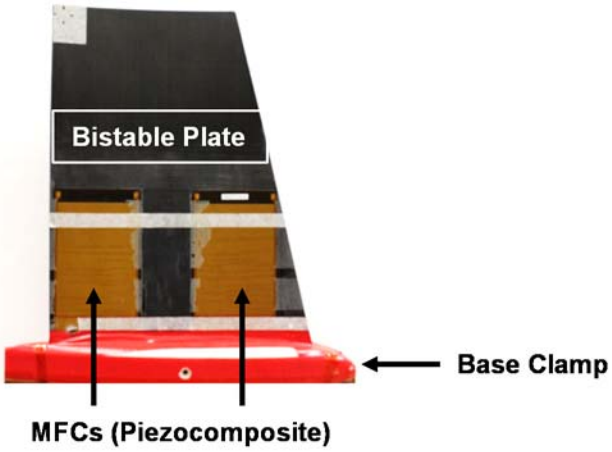

Figure 3-1: Clamped unsymmetric cross-ply bistable plate with unimorph MFCs.

The setup including the structure and the signal acquisition-generation-processing parts is presented in Figure 3-2.

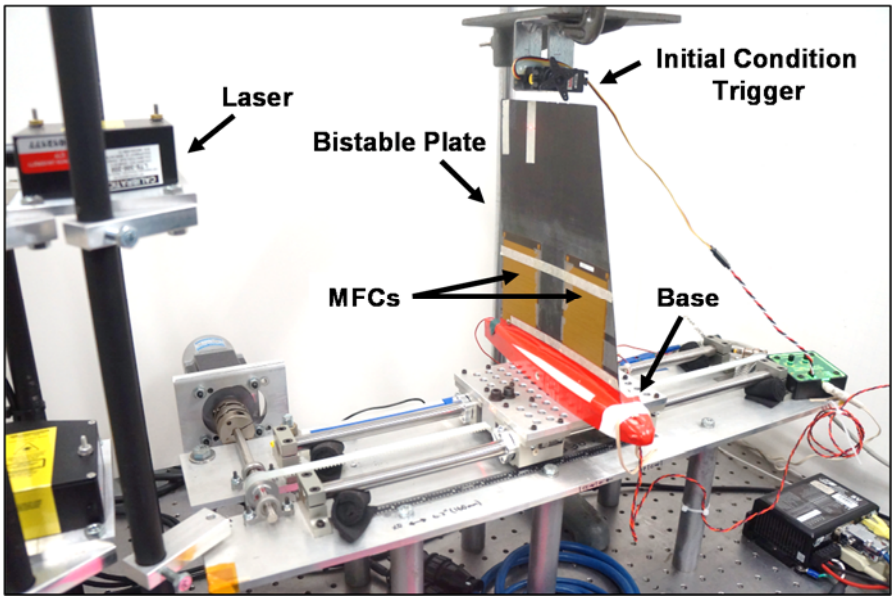

Figure 3-2: Experimental setup.

The controller is programmed using Simulink, a toolbox in MATLAB software. An algorithm written in dSPACE Control Desk software is used to implement the controller on a dSPACE 1104 real time control board. The tip displacement of the plate is measured with an MTI Instruments LTC-300-200-SA type laser displacement sensor. The output of the controller is fed to the MFC actuator using a TREK 2220 high voltage amplifier with 200x gain. The experimental

setup also has a servo actuated initial condition trigger placed near the tip of the plate. In addition, a push-back servo mechanism is placed at the same place to push the tip of the plate to its original position if the tip position is changed to the other stable equilibrium position during the experiment. The experimental setup is illustrated in Figure 3-3.

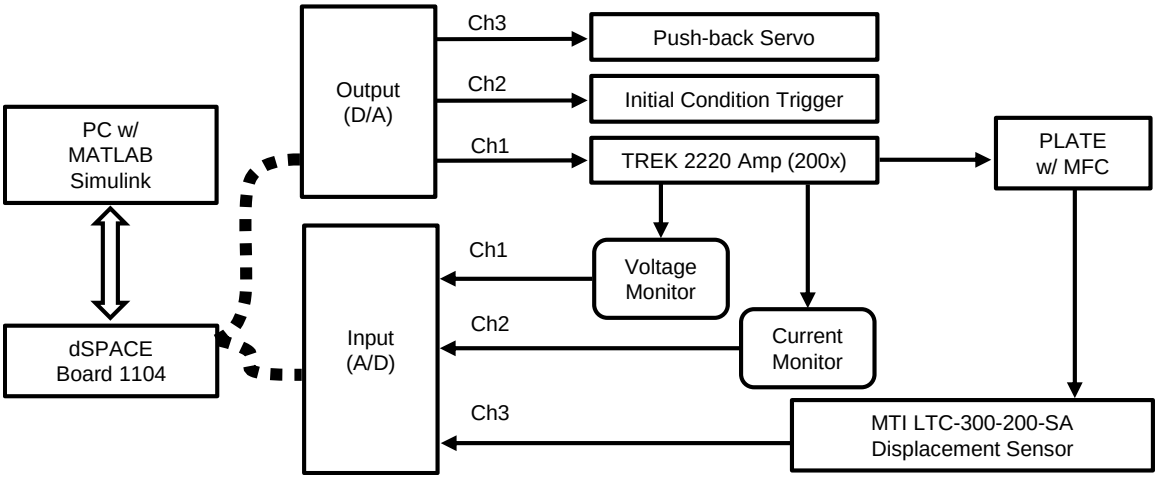

Figure 3-3: Diagram of the control experiment.

3.3. Assumed Linear Model around Stable Equilibria

Effective mass, stiffness and damping characteristics around stable equilibria are assumed. The single degree of freedom forced vibrations of the first bending mode of the assumed system can be represented by:

$$\ddot{w} + 2\zeta\omega_n \dot{w} + {\omega_n}^2 w = f(t) \tag{3.1}$$

where w is the tip displacement of the plate. The ζ and ω_n indicate the damping ratio and natural frequency respectively, and $f(t)$ is the mass-normalized forcing input.

The experimental and theoretical frequency responses are presented in Figure 3-4. The experimental response is deduced using cross power spectral density analysis where the input is the excitation voltage and the output is the tip displacement of the plate. Experimentally determined ω_n and ζ are entered into a second order model, and the identified analytical model is plotted in the figure.

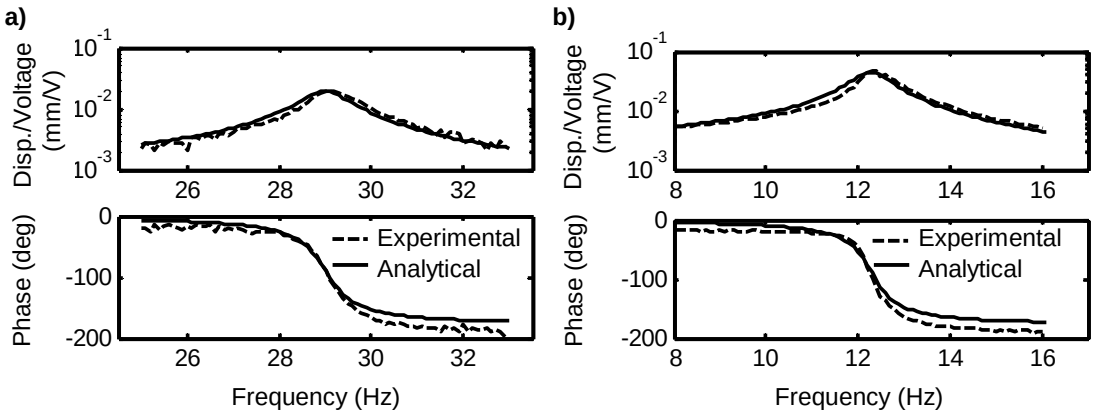

Figure 3-4: The frequency response of the structure around a) *State 1*, b) *State 2* to harmonic excitation of a) 50 Vpeak, b) 100 Vpeak.

As can be seen in Figure 3-4 (a) and (b), the magnitude response from the experiment and the analytically derived second order model show good agreement. Also, phase responses show good match except for a small phase offset. This discrepancy is due to the effect of piezoelectric and structural hysteresis. The identified model parameters are presented in Table 3-1. For a preliminary demonstration, the controller frequency is selected just above the structural natural frequency to exploit the resonant amplification. The damping ratio of the controller is selected as 50% for State 1 and 30% for State 2.

Table 3-1: Parameters for the bistable plate and the hybrid controller.

	Frequency	Damping Ratio	Gain
Structure - State 1	$\omega_n = 191.6$ rad/s	$\zeta = 0.038$	$g_n = 0.0072$ (mm/s^2)/V
Structure - State 2	$\omega_n = 81.05$ rad/s	$\zeta = 0.036$	$g_n = 0.0302$ (mm/s^2)/V
Controller - State 1	$\omega_f = 219.9$ rad/s	$\zeta_f = 0.50$	$g_f = 0.500$ V/mm
Controller - State 2	$\omega_f = 94.25$ rad/s	$\zeta_f = 0.30$	$g_f = 0.0700$ V/mm

3.4. Preliminary Experiments Showing Feasibility

First, a set of preliminary conventional control analyses are conducted on the passive bistable wing to understand the change in the dynamic behavior under control gains. Next, a simple demonstration is conducted where the plate is turned into an effectively monostable structure, or alternatively, both stable equilibrium positions can be reached actively from the other stable equilibrium with minimum control effort. Dynamic and monotonic forward and

reverse (Figure 3-5) snap-through is demonstrated in these experiments which show the effectiveness of the proposed HPF control scheme through piezoelectric actuation. The assumed parameters were presented in Table 3-1.

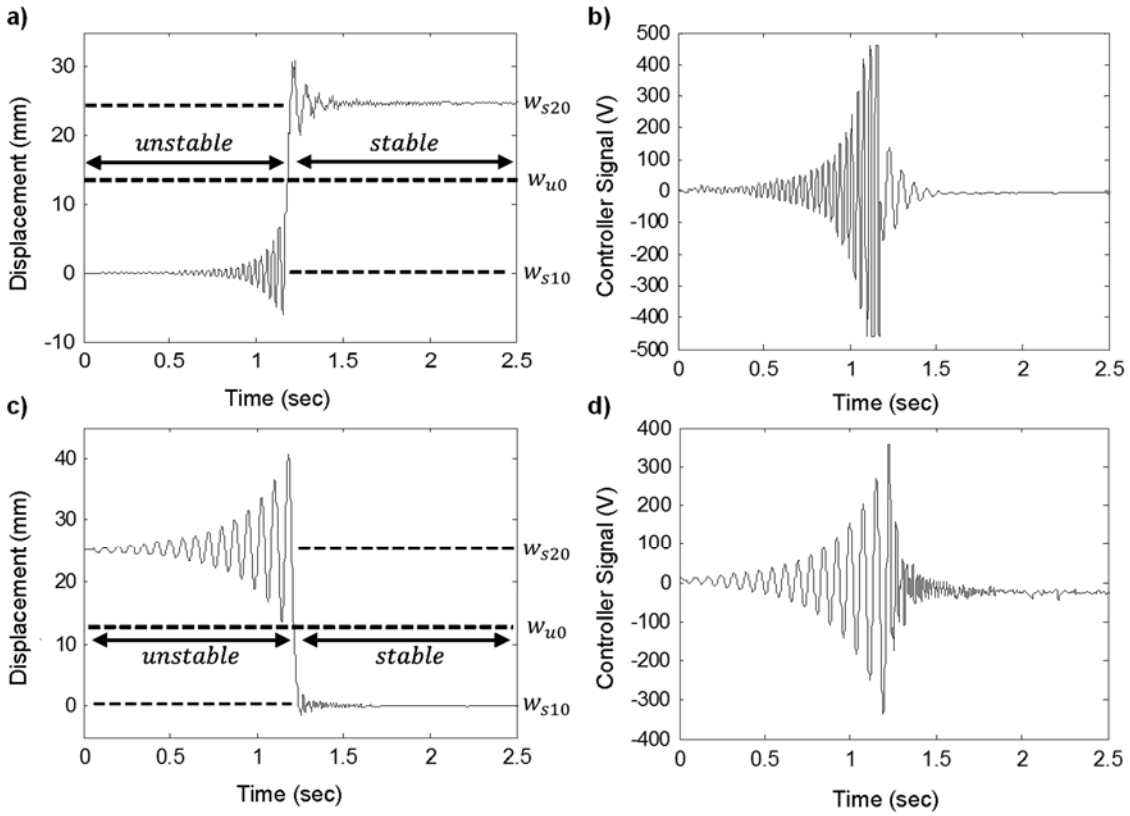

Figure 3-5: Transition from State 1 to State 2 using the HPF controller: a) Response, b) control effort. Transition from State 2 to State 1 using the HPF controller: c) Response, d) control effort.

In the figures, w_{s10} and w_{s20} indicate the stable equilibrium positions of State 1 and State 2 respectively. The label w_{u0} indicates the unstable equilibrium position. Figure 3-5 clearly demonstrates the feasibility of the proposed hybrid control scheme.

3.5. Parametric Analysis and Comparison to Simulations

A series of parametric tests are carried out to show the effect of controller parameters on the stability characteristics of the controlled bistable structure. Controller parameters such as frequency (ω_f), damping ratio (ζ_f) and gain (g_f), are swept in a wide range. The parametric tests are conducted for both operational modes of the hybrid controller.

3.6. Experimental Procedure

The experimental procedure is designed to conduct a three-parameter sweep in an automated manner. These parameters are swept in three nested loops. The controller frequency is changed in the innermost loop while the control gain is changed in the outermost loop. Response to each individual parameter set is analyzed using the recorded time history as shown in Figure 3-6.

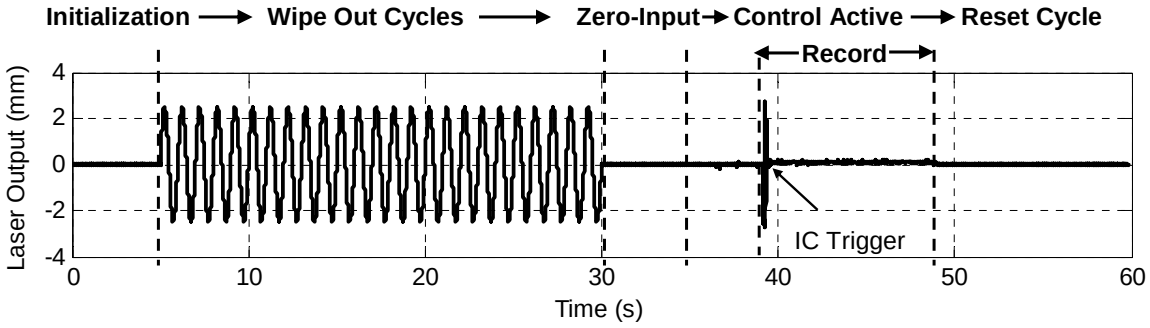

Figure 3-6: An example experimental time history for each control experiment.

The experimental procedure shown in Figure 3-6 is applied to each parameter set. There are initialization, wipe-out, zero-input, control active, recording, and reset periods. In the initialization period, the parameters are updated. Then, the wipe-out cycles introduce a pure sinusoidal input with a magnitude of 500V at a frequency of 1 Hz to remove the hysteresis memory. Next, the offset values are updated by having a zero-input period. Next, the controller is activated at the beginning of the control-active period. The procedure mentioned above is mostly the same for both PPF and NPF controllers. For the NPF controller, the data collection starts as soon as the controller is activated. However, for the PPF controller, there is another time interval before the application of the external trigger. Once the trigger is applied, the recording window of the PPF starts. Finally, there is a reset period for the necessary changes in the algorithm before the start of the next cycle. During this period, the push-back servo forces the bistable plate back to the desired equilibrium state (in case cross-over occurred.)

3.7. PPF Stability Comparison

The theoretical stability behavior of the PPF controller is compared to the experimental results. Figure 3-7 shows the stability of both experimental and the theoretical results for varying controller parameters. The black and red points represent the desirable (stable) and undesirable (unstable) responses respectively. For the theoretical response, the controller frequency is normalized with the system natural frequency, and this metric is given by $\omega_r = \omega_f/\omega_n$. For the experimental response, such normalization is not practical because the so-called natural frequency of the system varies. Hence, the controller frequency is represented by f, and its unit is Hertz.

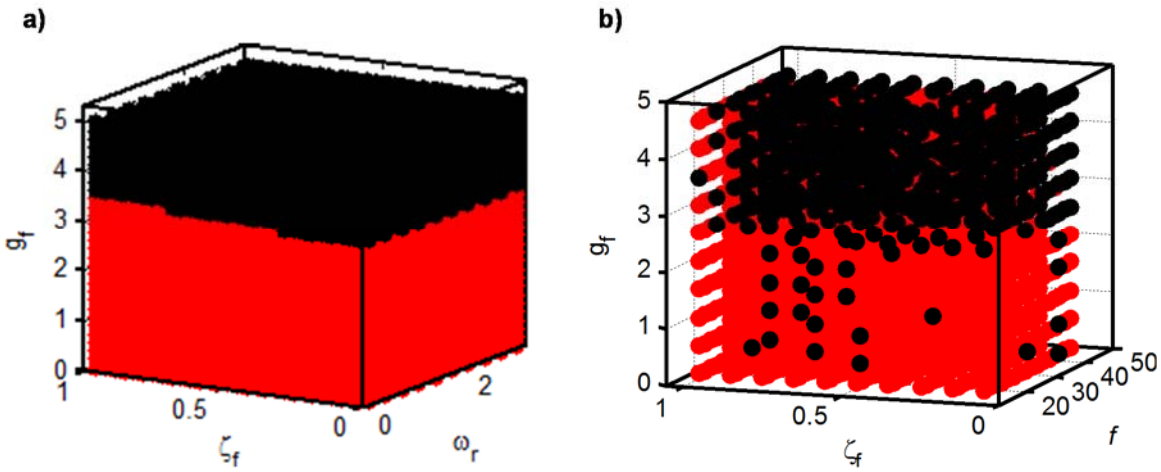

Figure 3-7: Comparison of stability results of the PPF controller, from a) numerical simulations, b) experiments.

Theoretically, the stability condition of the PPF controller depends solely on the controller gain, as shown in Figure 3-7 (a). Also, the monotonic color distribution implies that the controller dynamics have no effect on the system stability. The experimental result shown in Figure 3-7 (b) is in generally good agreement with the theoretical results. However, there are some unstable parameters in the predicted stable region in Figure 3-7 (b) that are assumed to occur due to mode coupling effects and the geometric nonlinearities. The response at these parameter sets are not repeatable due to the hysteretic behavior of the piezo-composite plate. Figure 3-8 shows the time response for two of these parameter sets.

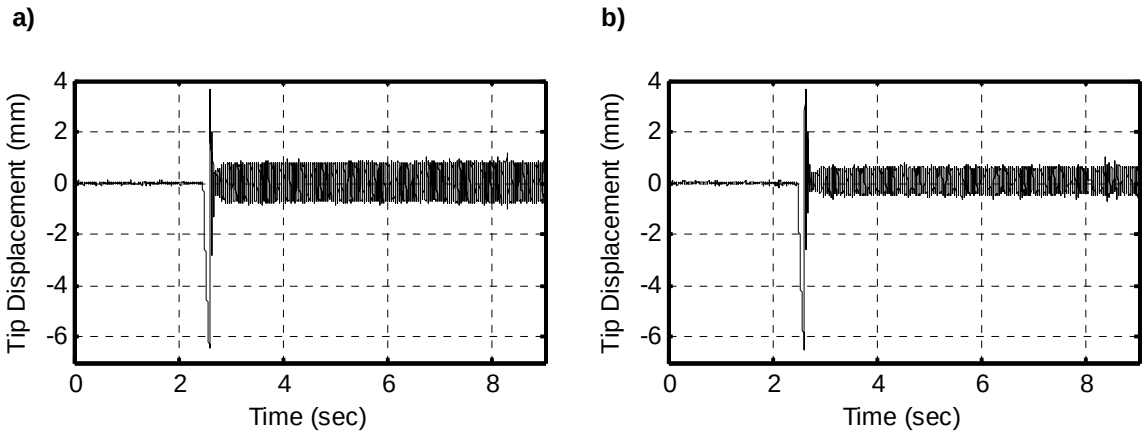

Figure 3-8: Example time responses for the unstable behavior observed in the theoretically-stable region a) $\omega_r = 1.19$, $\zeta_f = 1$, and $g_f = 0.1$, and b) $\omega_r = 1.47$, $\zeta_f = 0.1$, and $g_f = 1.6$.

3.8. NPF Stability Comparison

The destabilizing characteristic of the NPF controller is also tested experimentally. The wide unstable bandwidth of the NPF controller is validated experimentally, and the effects of the controller parameters are discussed in comparison to the theoretical analysis. Figure 3-9 shows the stability behavior of the NPF controller. The blue points show desirable (unstable) parameter sets, and the black points are undesirable (stable) parameter sets.

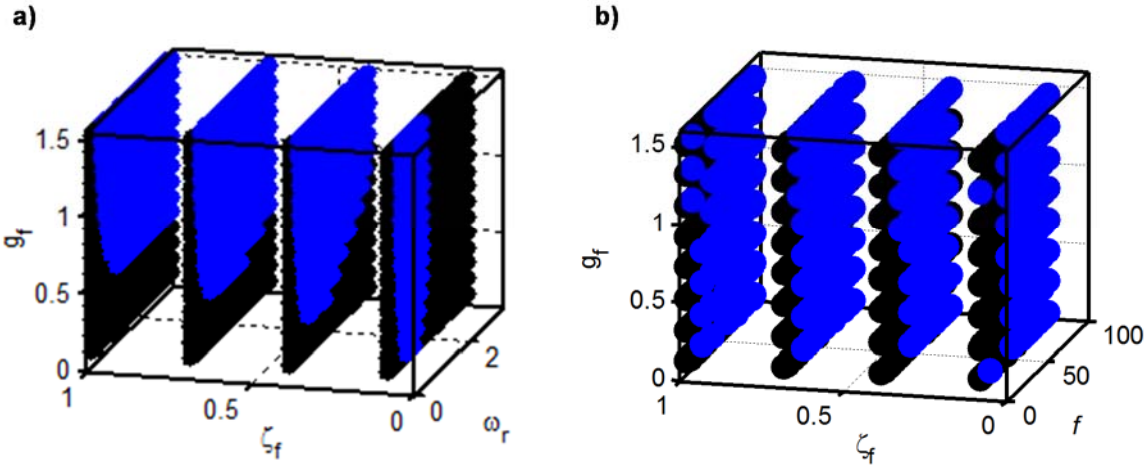

Figure 3-9: Comparison of stability results of the NPF controller, from a) numerical simulations, b) experiments.

As can be seen in Eqs. (2.17) and (2.18), the stability of the NPF controller depends highly on every parameter of the controller and the structure. Small stable gain margins are observed in

Figure 2-9 and in Figure 3-9 (a). The black points represent the undesirable parameters, existing in low gain regions of Figure 3-9 (a). The desirable points, blue points, cover almost all damping ratios and excitation frequencies for different controller gains except low frequencies. This behavior is also observed in experimental results, as shown in Figure 3-9 (b). The experimental results validate observations made from the theoretical analyses.

3.9. PPF Energy Results

The experimental energy transferred in both PPF and NPF modes of the HPF controller is calculated using measured excitation voltage ($V\ (t)$) and current ($I(t)$). The power is integrated using the numerical trapezoidal rule given by,

$$E = \int_0^T V\ (t)\ I(t)\ dt. \tag{3.2}$$

The experimental tests of the PPF controller are conducted in two parts. In the first part, the damping ratio is kept constant to examine the effect of the controller frequency and gain on energy consumption. Figure 3-10 shows the experimental energy calculated for constant $\zeta_f = 0.4$. The parameters focus around the natural frequency since the controller exploits the resonance of the structure. Also, most of the energy variance is expected in that frequency range. The controller gain ranges from 0 to 3 to see the effect of gain on energy transfer of the controller.

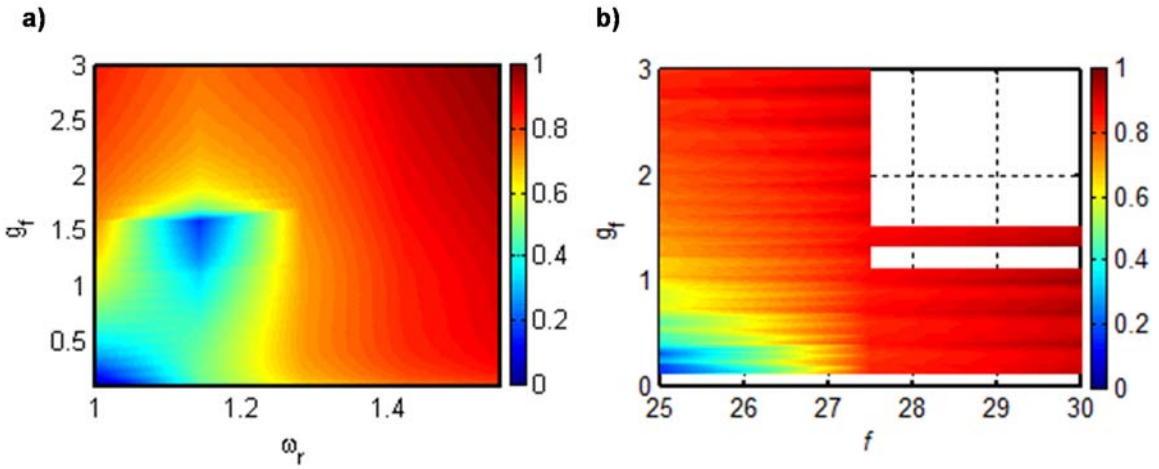

Figure 3-10: Comparison of energy results of PPF control a) numerical simulation, and b) experiment for $\zeta_f = 0.4$.

As can be seen in Figure 3-10 (b), the energy transfer to suppress the response is low when the controller frequency is around the natural frequency of the structure and the controller gain is low. The controller frequency close to the system natural frequency provides quick suppression which reduces the additional oscillation and consequently the work done by input excitation against non-conservative forces. As for the controller gain, the work extracted from the structure increases with the increase in controller gain to create a quick suppression. This leads to a higher energy requirement for the controller to suppress the response, as can be seen in Figure 3-10 (b). The equivalent simulation in Figure 3-10 (a) shows similar energy characteristics.

The experimental energy variance by the change of controller gain and natural frequency for constant gain of $g_f = 0.3$ is represented in Figure 3-11 for the PPF controller.

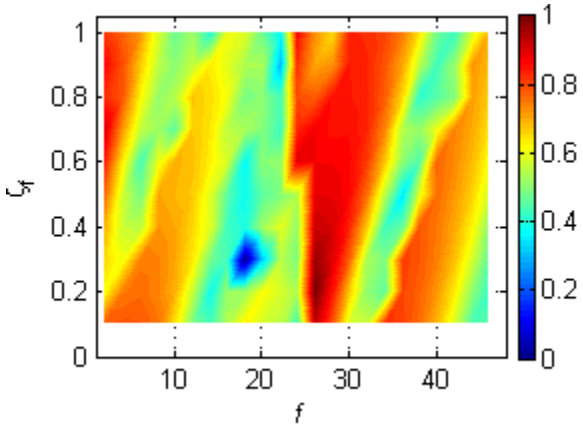

Figure 3-11: Experimental energy results of the PPF controller for $g_f = 0.3$.

The energy characteristics are not showing linear two-mode system behavior. The energy levels fluctuate along the controller frequency. Also, the energy distribution for constant controller frequency is not showing uniform increase or decrease. This is due to the constantly changing natural frequency of the structure.

3.10. NPF Energy Results

The experimental energy results for the NPF controller are shown in Figure 3-12. The controller frequency and damping ratio range from 10 to 60 Hz and 0 to 2, respectively. The constant controller gains are selected as 3 and 2 for simulation and experiment respectively.

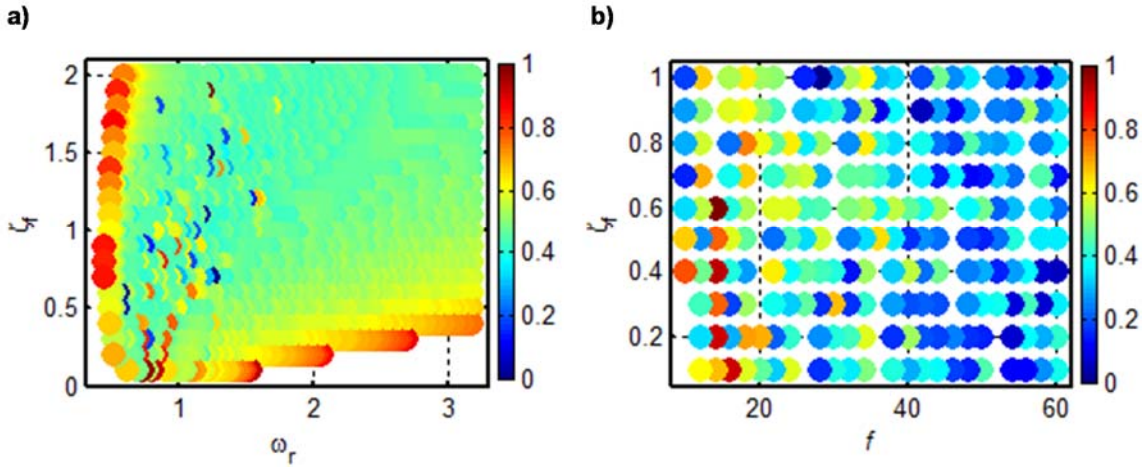

Figure 3-12: Comparison of energy results of the NPF controller a) numerical simulation with $g_f = 3$, b) experiment with $g_f = 2$.

Although, a uniform energy variance is not observed in Figure 3-12, the energy difference in a wide parameter reveals similar trends. First, there is an inverse relation between energy consumption and the controller frequency. This trend can be seen in Figure 3-12 (a). Second, the energy consumption is not varying significantly as the damping ratio varies. Figure 3-12 (a) shows similar non-uniform energy characteristics.

3.11. Conclusions

The experimental analysis demonstrates the feasibility of the hybrid controller as a strategy to control bistable structures. The stability regions seen in the theoretical results are also observed in the experimental behavior.

Discrepancies in experimental energy results are observed when compared to the simulation results. This is assumed to be due to the nonlinearity of the actuator and the composite laminate.

CHAPTER 4:
CONCLUSIONS AND FUTURE WORK

This thesis presented a detailed analysis of the hybrid controller as a strategy to control the cross-well motion of bistable structures. This chapter first summarizes the conclusions from previous chapters. Next, the academic publications that stemmed from the current research are listed. Finally, recommendations are made for the future direction of the research.

4.1. Summary of Results

Chapter 2 presented theoretical stability results that can be used to design the hybrid controller for different considerations such as simplicity and performance. Also the energy and performance characteristics of the hybrid controller as functions of controller parameters are provided.

Chapter 3 presented experimental results to show the feasibility of the hybrid control idea. Control authority and energy characteristics are shown for both modes. Also, experimental stability and energy analyses showed a reasonable match compared to the theoretical results.

4.2. Related Publications

Portions of this thesis have been presented at professional conferences. Also, a journal article is pending. These works are the foundation for this thesis. Below is a list of related conference papers, presentations and the journal article.

- Bilgen, Onur, Simsek, Mehmet R. and Arrieta, Andres F. "Minimum Energy Cross-Well Actuation of Bistable Piezocomposite Unsymmetric Cross-Ply Plates." ICAST2014: 25nd International Conference on Adaptive Structures and Technologies October 6-8th, 2014, The Hague, The Netherlands.
- Simsek, Mehmet R. and Bilgen, Onur. "Hybrid Position Feedback Control of Bistable Structures", AIAA Science and Technology Forum and Exposition (AIAA SciTech 2016).

- Simsek, Mehmet R. and Bilgen, Onur. in review "Hybrid Position Feedback Control of Bistable Structures", submitted to AIAA Journal.

4.3. Future Work

A nonlinear model can be developed to cover the nonlinear behavior of the bistable plate. Also, a nonlinear control method can be considered as new strategy to achieve higher performance.

In addition, the stability needs to be analyzed under base excitation. Moreover, controller performance needs to be investigated under external disturbances caused by different types of airflow such as normal, gust and turbulent cases.

REFERENCES

[1] R. B. Williams, G. Park, D. J. Inman, and W. K. Wilkie, "An overview of composite actuators with piezoceramic fibers," *Proceeding of IMAC XX,* pp. 4-7, 2002.

[2] M. W. Hyer, "Some observations on the cured shape of thin unsymmetric laminates," *Journal of Composite Materials,* vol. 15, pp. 175-194, 1981.

[3] C. G. Diaconu, P. M. Weaver, and F. Mattioni, "Concepts for morphing airfoil sections using bi-stable laminated composite structures," *Thin-Walled Structures,* vol. 46, pp. 689-701, 2008.

[4] M. W. Hyer, "Calculations of the room-temperature shapes of unsymmetric laminates," *Journal of Composite Materials,* vol. 15, pp. 296-310, 1981.

[5] K. D. Potter and P. M. Weaver, "A concept for the generation of out-of-plane distortion from tailored FRP laminates," *Composites Part A: Applied Science and Manufacturing,* vol. 35, pp. 1353-1361, 2004.

[6] E. Kebadze, S. Guest, and S. Pellegrino, "Bistable prestressed shell structures," *International Journal of Solids and Structures,* vol. 41, pp. 2801-2820, 2004.

[7] S. Daynes, K. Potter, and P. Weaver, "Bistable prestressed buckled laminates," *Composites Science and Technology,* vol. 68, pp. 3431-3437, 2008.

[8] S. Daynes, P. Weaver, and J. Trevarthen, "A morphing composite air inlet with multiple stable shapes," *Journal of Intelligent Material Systems and Structures,* p. 1045389X11399943, 2011.

[9] M.-L. Dano and M. Hyer, "SMA-induced snap-through of unsymmetric fiber-reinforced composite laminates," *International Journal of Solids and Structures,* vol. 40, pp. 5949-5972, 2003.

[10] M. R. Schultz, M. W. Hyer, R. B. Williams, W. K. Wilkie, and D. J. Inman, "Snap-through of unsymmetric laminates using piezocomposite actuators," *Composites science and technology,* vol. 66, pp. 2442-2448, 2006.

[11] A. Arrieta, D. Wagg, and S. Neild, "Dynamic snap-through for morphing of bi-stable composite plates," *Journal of Intelligent Material Systems and Structures,* p. 1045389X10390248, 2010.

[12] A. Senba, T. Ikeda, and T. Ueda, "A two-way morphing actuation of bi-stable composites with piezoelectric fibers," in *51st AIAA/ASME/ASCE/AHS/ASC Structures, Structural Dynamics, and Materials Conference 18th AIAA/ASME/AHS Adaptive Structures Conference 12th*, 2010, p. 2744.

[13] O. Bilgen, M. R. Simsek, and A. F. Arrieta, "Minimum Energy Cross-Well Actuation of Bistable Piezocomposite Unsymmetric Cross-Ply Plates," in *ICAST2014: 25th International Conference on Adaptive Structures and Technologies*, 2014.

[14] O. Bilgen, Y. Wang, and D. J. Inman, "Electromechanical comparison of cantilevered beams with multifunctional piezoceramic devices," *Mechanical Systems and Signal Processing,* vol. 27, pp. 763-777, 2012.

[15] E. F. Crawley and E. H. Anderson, "Detailed models of piezoceramic actuation of beams," *Journal of Intelligent Material Systems and Structures,* vol. 1, pp. 4-25, 1990.

[16] C. J. Goh, "Analysis and control of quasi distributed parameter systems," California Institute of Technology, 1983.

[17] C. Goh and T. Caughey, "On the stability problem caused by finite actuator dynamics in the collocated control of large space structures," *International Journal of Control,* vol. 41, pp. 787-802, 1985.

[18] J. Fanson and T. K. Caughey, "Positive position feedback control for large space structures," *AIAA journal,* vol. 28, pp. 717-724, 1990.

[19] J. Dosch, J. Calamita, and D. Inman, "Performance of a programmable structure [1919-17]," in *PROCEEDINGS-SPIE THE INTERNATIONAL SOCIETY FOR OPTICAL ENGINEERING*, 1993, pp. 151-151.

[20] M. I. Friswell, D. J. Inman, and R. W. Rietz, "Active damping of thermally induced vibrations," *Journal of Intelligent Material Systems and Structures,* vol. 8, pp. 678-685, 1997.

[21] D. J. Leo and D. J. Inman, "Pointing control and vibration suppression of a slewing flexible frame," *Journal of guidance, control, and dynamics,* vol. 17, pp. 529-536, 1994.

[22] P. A. Tarazaga, D. J. Inman, and W. K. Wilkie, "Control of a space rigidizable inflatable boom using macro-fiber composite actuators," *Journal of Vibration and Control,* vol. 13, pp. 935-950, 2007.

[23] A. Meitzler, H. Tiersten, A. Warner, D. Berlincourt, G. Couqin, and F. Welsh III, "IEEE standard on piezoelectricity," ed: Society, 1988.

[24] J. L. Donald and D. Leo, "Engineering analysis of smart material systems," *Hoboken, New Jersey: John Wiley & Sons,* 2007.

[25] kridnix. (2014, April 22, 2016). *2 5 Permittivity and Displacement*. Available: https://www.youtube.com/watch?v=DkqdNUTMrHc

[26] S. M. Coorp. (22 Mar). *MFC actuation mode*. Available: http://www.smart-material.com/media/images/MFCP1-mode-small.png

[27] S. M. Coorp. (22 Mar). *P1 Mode MFC with micro view*. Available: http://www.smart-material.com/media/images/MFC-P1-Layout.png

[28] O. Bilgen, A. F. Arrieta, M. I. Friswell, and P. Hagedorn, "Dynamic control of a bistable wing under aerodynamic loading," *Smart materials and structures,* vol. 22, p. 025020, 2013.

VITA

EDUCATION

- Old Dominion University, Norfolk, VA — 05.2016
  M.Sc. in Mechanical Engineering (GPA 4.00)
  Thesis: "Hybrid Control for Minimum Energy Piezoelectric Actuated Bistable Wing"
- Kocaeli University, Kocaeli, Turkey — 06.2012
  B.Sc. in Mechatronics Engineering (with Honor GPA 3.21)
  Areas of Concentration: *Robotics and Automation*
- Bochum University of Applied Science — 08.2011
  B.Eng. in Mechatronics Engineering (GPA 1.7 (in German System))
  Areas of Concentration: *Automation and Vibrational Analysis of Structure*
  Thesis: "*Construction of Electrical Cylinder-Based Spring-Damper System*"

ACADEMIC EXPERIENCE/HIGHLIGHTS

- Old Dominion University, Norfolk, VA — 09.2014-05.2015
  Graduate Advisor-Senior Design Project
  Prosthetic Arm Design, Advised for Control and Circuit Design Part
- Old Dominion University, Norfolk, VA — 06.2014-08.2014
  Co-Mentor- Smart Systems Summer Camp (S3C), Summer 2014
  Mentored two high school students on scientific research and experimentation.
- Turkish Military Academy, Ankara, Turkey — 01.2013-06.2013
  Lecturer- Dynamics I
  Revised the Syllabus, prepare the exam materials and administered all grades for Junior classes.

EMPLOYMENT/INTERNSHIPS

- Telfleks LLC, Istanbul, Turkey — 12.2011-07.2012
  Project Engineer in R&D Project
  Automation of a manual controlled industrial coil winding machine with servo system.
  Implementation of length measurement system to the machine.
- Laboratory of Control and Regulation Technology, Bochum University of Applied Science, Bochum, Germany — 07.2010-08.2010
  Intern
  Implementation of the real device to adjust the system (Loading Crane, Fillings Level, Turntable, Ball Rocker)
- Laboratory of Applied Informatics, Bochum University of Applied Science, Bochum, Germany — 09.2010-02.2011
  Intern

Fundamentals Application with AVR-Experiment Cards (Configuring of LCD (Hitachi-HD44780).
Writing the Character on LCD, A/D Converter, Serial Interface UART-USART, and PWM.

- Laboratory of Informatics (Technical Image Processing), Bochum University of Applied Science, Bochum, Germany — 09.2010-02.2011
  Intern
  Recognition of a work piece using the industrial camera (Omron ZFX Vision camera) and warn the operator with LED.
- Laboratory for Automation Technics and Robotics), Bochum University of Applied Science, Bochum, Germany — 07.2010-02.2011
  Intern
  Applications with Simatic Manager Step 7 (configuration of PLC, Profibus and MPI bus communication of S7-300 and s7-400, Master- Slave Controlling of seven-segment display).
- CEL-MER LLC., Kocaeli, Turkey — 07.2010-08.2010
  Intern
  High Power AC-Machine Drive through Electrical Panels using Star-Delta Transformation.
  Tracking the machining process done by Drilling, Universal Milling Machine and Lathe.
- HAR-TEK, Istanbul, Turkey — 06.2010-07.2010
  Intern
  AC Motor V/f and PID Control over Driver PLC Application for Servo- and AC-Driver

AWARDS

- Full Financial Support for Ph.D. Study in U.S. from Turkish Military Academy
- Second Best Degree in Examination for Double Degree Program
- Honor Student

LANGUAGES

- Turkish - native language
- English - speak fluently, read/write in high proficiency
- German - speak fluently, read/write in high proficiency (C1-certified by KMK)

SKILLS/SOFTWARE

SKILLS

- Matlab
- Simulink
- Solidworks

SOFTWARE

- Data Acquisition
- Control System Design
- Signal Processing

- Comsol
- Proteus
- Mathematica
- dSPACE/Control Desk
- MS OFFICE
- AVR STUDIO
- WinFACT Boris
- Labview
- AutoCAD
- Experimenting
- Microcontroller Programming
- Structural Analysis
- Mathematical Modelling
- Robot Kinematics and Dynamics